SAND2011-9409C

DSMC Simulations of the Plasma Bombardment on Io's Sublimated and Sputtered Atmosphere

Chris H. Moore*, Andrew C. Walker†, David B. Goldstein‡, Philip L. Varghese§, and Laurence M. Trafton**
University of Texas, Austin, TX, Zip 78712

and

Neal Parsons†† and Deborah A. Levin‡‡
Pennsylvania State University, University Park, PA, Zip 16802

The DSMC method is used to model the interaction of the jovian plasma torus with Io's SO_2 sublimation and sputtered atmosphere just prior to eclipse. The SO_2 frost sublimes on the warm dayside and photo and neutral chemistry, the dominant source of the daughter species (SO, O_2, O, and S) are included. To model the plasma interaction with the sublimation atmosphere, a two-timestep method is utilized in which the neutrals are assumed to be stationary while electrons and ions are moved and collided over a much smaller timestep. The dominant ion-neutral interactions (non-reactive and resonant charge exchange) are included. Sputtering of SO_2 molecules from the frost-covered surface is dependent on the incident ion energy and the surface frost temperature. Io's surface is assumed to be uniformly covered by SO_2 surface frosts with the temperature computed based on radiative equilibrium with insolation. We investigate the effect of the plasma interaction with Io's atmosphere on its composition and structure, its circumplanetary winds, and the escape rate of material from Io to the plasma torus. The dense sublimation atmosphere reduces sputtering from SO_2 surface frosts over much of the dayside; however, sputtering was found to be a significant contributor to the nightside atmosphere. The plasma pressure on the sublimation atmosphere has a substantial effect on the day-to-night winds. Not only does the plasma pressure induce an overall retrograde wind in Io's atmosphere just prior to entry into eclipse, but the atmospheric scale height is reduced by the plasma pressure on the trailing hemisphere. Molecular oxygen is a minor species on the dayside but is found to be the dominant nightside species because it is non-condensable and the loss rates due to atmospheric escape or dissociation are slow.

I. Introduction

Io, the innermost Galilean satellite of Jupiter, exhibits a wide variety of complex phenomena such as interaction with Jupiter's magnetosphere, volcanic activity, and a rarefied multi-species sublimating and condensing atmosphere with an ionosphere. Jupiter's magnetosphere is larger and stronger than any planet in the solar system and is tilted by ~10° relative to Jupiter's rotation axis. In the vicinity of Io, the Jovian magnetic field is perturbed by Io;[1] furthermore, Io does not have an intrinsic magnetic field.[2] An excellent review of the Jovian magnetosphere and the torus is given in Ref. 3 and 4. Material from Io's atmosphere continually supplies an ionized ring of plasma called the Io plasma torus which co-rotates with Jupiter. The Io plasma consists predominantly of O^+, S^+, and electrons and sweeps past Io at ~57 km/s since Io's orbital period is slower than Jupiter's rotational period. The plasma, confined

*Nanoscale and Reactive Processes, Sandia National Laboratories, Albuquerque, NM, 87185-1322, e-mail: chmoore.314@gmail.com
† PhD Candidate, Department of Aerospace Engineering, University of Texas, 1 University Station C0600, Austin TX, 78712, e-mail: andrew.walker@mail.utexas.edu
‡ Professor, Department of Aerospace Engineering, University of Texas, 1 University Station C0600, Austin TX, 78712, e-mail: david@ices.utexas.edu
§ Professor, Department of Aerospace Engineering, University of Texas, 1 University Station C0600, Austin TX, 78712, e-mail: varghese@mail.utexas.edu
** Senior Research Scientist, Department of Astronomy, University of Texas, 1 University Station C1402, Austin TX, 78712, e-mail: lmt@astro.as.utexas.edu
†† University Graduate Fellow, Department of Aerospace Engineering, Pennsylvania State University, University Park, PA 16802, e-mail: nsp5088@psu.edu
‡‡ Professor, Department of Aerospace Engineering, Pennsylvania State University, University Park, PA 16802, e-mail: dal16@psu.edu

to move along the rotating Jovian magnetic field lines, interacts with Io's atmosphere as it sweeps past the satellite, ionizing neutrals in Io's atmosphere via collisions. These new ions (and electrons) are then accelerated by the rotating field lines to resupply the torus. In eclipse, the only significant source of the observed [OI] emission is the interaction of electrons (and ions) from the plasma torus with Io's atmosphere. Additionally, Voyager 1 detected a ~6 MA current of high energy electrons along the Io flux tube which extends between Io and the Jovian North and South Poles. These field-aligned electrons create a UV auroral footprint in Jupiter's ionosphere[5] and triggers Jovian decametric radio emission.[6]

The Io plasma torus has a cold inner torus from 4.9-5.3 R_J (R_J is Jupiter's radius), a "ribbon" of warmer plasma from 5.5-5.9 R_J, and a warm region out to 7.5 R_J.[7,8] At Io's orbit (5.9 R_J), the thermal electrons in the plasma have a temperature of ~5eV and hence a mean energy, E, of 7.5eV,[9] and a number density of ~3600 m^{-3};[1] though both these quantities vary with Io's System III longitude as Io passes through the plasma "ribbon".[10] Charged particles in the torus are confined on the Jovian magnetic field lines; however, due to the centrifugal "force" of rotation about Jupiter, the torus equator is inclined by only 7° relative to Io's orbital plane as compared to 10° for the Jovian magnetic equator.[11]

Io's interaction with the plasma torus has been simulated numerous times using the magnetohydrodynamic (MHD) equations.[12-14] The co-rotational electric field is altered by collisions in Io's ionosphere, causing most of the plasma flux tubes to divert around Io and inducing a twist of the electric field across Io.[15] Additionally, the co-rotational electric field generates the observed ~10 MA current which is thought to be carried to Jupiter's poles along field-aligned Alfvén wings.[15,16]

Combi, *et al.* developed a 3D global, multi-scale magnetohydrodynamic (MHD) simulation for a one fluid plasma that accounted for mass-loaded flow.[14] They qualitatively reproduced the Galileo fly-by plasma and field observations in Io's wake[1] such as the plasma density peak and the plasma pressure; however, they did not quantitatively match detailed features such as the magnitude of the double-peaked magnetic field disturbance in the wake.

Saur *et al*. used an electrodynamic model and calculated the density, velocity and temperature of thermal electrons and one representative ion species, and the electric field near Io in a self-consistent manner. [4,15,17,18] The Hall effect was found to twist the plasma flow around Io and cause a brighter OI] 1356 Å equatorial auroral spot on the anti-Jovian side than the sub-Jovian side, as observed.[17] They further attributed the origin and structure of the double peak magnetic field observed in Io's wake to diamagnetic and inertia currents.[18] Finally, they found that Io's atmosphere should be longitudinally asymmetric due to the drag force of the plasma, with the upstream scale height being significantly smaller than the downstream scale height.[18]

More recently, Lipatov and Combi performed a 3D hybrid simulation of the magnetic and electric environment about Io using a kinetic description for the ion motion and MHD equations to solve for the electron motion.[19] Their model was able to account for a more realistic anisotropic ion velocity distribution, charge-exchange, photo-ionization processes, and solve for the magnetic and electric fields self-consistently. They obtained good agreement to the Galileo I0 flyby data and found that the plasma flow around Io was strongly affected by the whistler and quasi-stationary Alfvén waves. A major finding was that the finite ion gyroradius results in an asymmetrical boundary layer near the ionosphere of Io and that the observed inverse structure of the magnetic field is due to the kinetic behavior of the ions.[19]

Dols *et al*. modeled the local interaction between Io's neutral corona and the plasma torus including ionization, charge exchange, and recombination of the SO_2, SO, O, and S neutral gas.[20] Comparison of their model results to Galileo observations of the plasma in Io's wake led them to conclude that molecular SO_2 chemistry dominates the interaction, SO_2^+ is the main ion produced near Io, the thermal torus electrons are not a sufficient ionization source and non-thermal field-aligned electron beams near Io must be important, and the neutral loss rate from Io is dominated by resonant charge exchange.[20] In the current work, the DSMC method is used to model the interaction of the jovian plasma torus with Io's SO_2 sublimation atmosphere. An external jovian magnetic and a co-rotational electric field are applied and used to calculate the ion movement. The model includes the momentum imparted by the plasma flow onto the atmosphere, plasma chemistry, and ion induced sputtering of the SO_2 frost that covers Io's surface. We investigate the circumplanetary winds formed in Io's atmosphere and the composition and structure of Io's atmosphere.

II. Model

A. Plasma Model

Jupiter's magnetic field sweeps a thermal plasma torus of predominately O^+ and S^+ ions past Io at ~57 km/s. The

plasma, confined to move along the rotating jovian magnetic field lines, interacts with Io's atmosphere as it sweeps past the satellite, ionizing, dissociating and heating the neutrals in Io's atmosphere via collisions. Above the exobase, fast neutrals and ions created by the plasma interaction can escape Io and resupply the torus. Furthermore, after undergoing collisions within Io's atmosphere, plasma particles are re-accelerated by the field lines so that further energetic interactions may occur. It is this interaction, along with photo-chemistry that likely produces the majority of SO_2 daughter products (SO, O_2, S, and O) in Io's atmosphere (volcanic plumes and surface sputtering are also sources for the SO_2 daughter products).

In order to have a more accurate model of Io's atmosphere for simulation of the aurora, the interaction of thermal torus ions and electrons with Io's neutral atmosphere is simulated in the planetary DSMC code. However, due to the large differences in timescales it was necessary to substep the plasma interaction within the overall DSMC code. This allowed for the gas to be simulated at a larger gas timestep and then, holding the gas fixed, simulate the plasma interaction with the standard DSMC routine at a much smaller timestep.

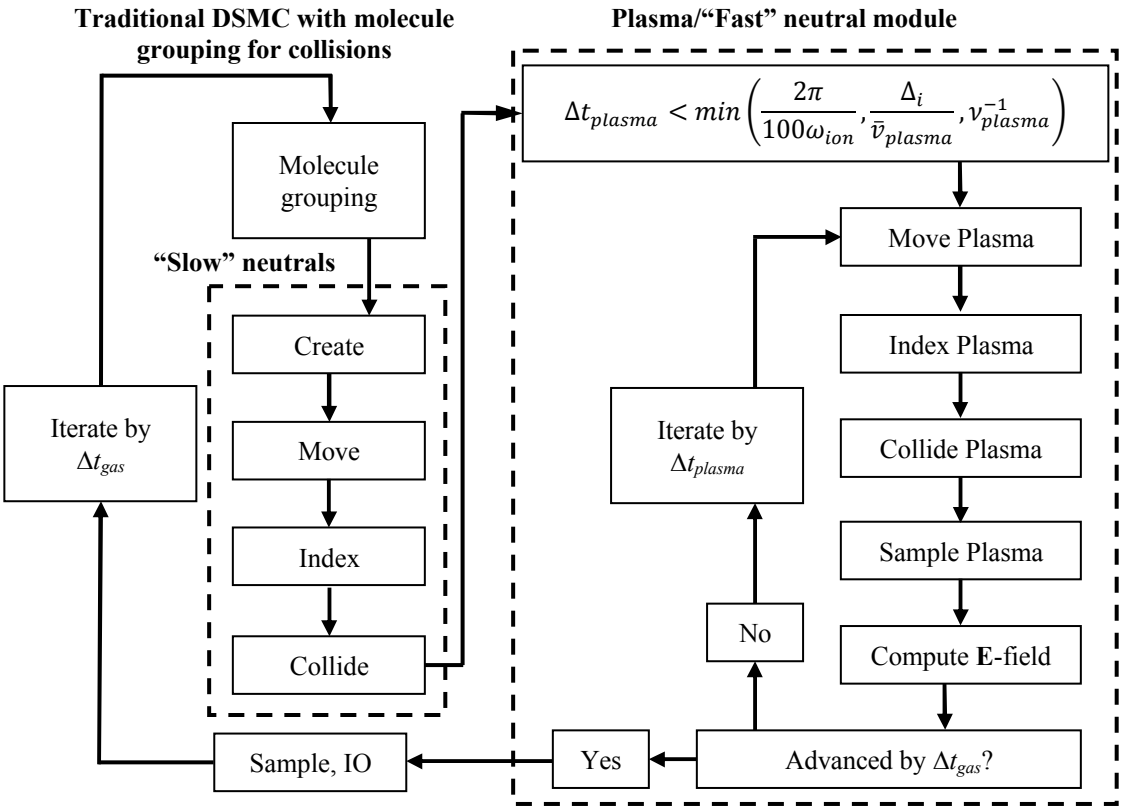

Figure 1. Flowchart of the DSMC method with a plasma/"fast" neutral sub-timestep routine. Note that for clarity only the plasma timescales are shown in sub-timestep routine.

Figure 1 shows a flowchart of the current implementation for the plasma substep routine performed after the neutral gas has moved and collided during the current timestep. The plasma timestep is much smaller than the neutral timestep and therefore requires many iterations to simulate the same time interval as the neutral timestep; however, since the plasma density is several orders of magnitude lower than the neutral gas density (except above the exobase), the neutral gas and plasma routines take roughly the same amount of computational time. In addition to the plasma substepping, fast neutrals produced by collisions with the charged particles (typically due to charge exchange) are grouped into the "plasma" molecule structure and are simulated on the "plasma" timestep. This allows for better computational efficiency since it prevents very large $(\sigma_{Tot} V_{rel})_{max}$ from occurring during the neutral-neutral collision step. It also allows for the use of our collision limiter scheme for the slow neutral–neutral collisions which do not, in general, chemically react.[21]

1. Charged Particle Motion

During the plasma substep routine, the charged particles are moved each plasma timestep accounting for gravity and the Lorentz force:

$$\vec{a} = \frac{d^2\vec{x}}{dt^2} = -g\left(\frac{R_{Io}}{r}\right)^2 \widehat{e_r} + \frac{eZ}{m}\left(\vec{E} + \vec{v} \times \vec{B}\right), \tag{1}$$

where g is the gravitational acceleration at Io's surface, R_{Io} is Io's radius, r is the radial position of the particle relative to the center of the satellite, $\widehat{e_r}$ is the radial unit vector, eZ is the charge of the particle, m is the mass of the particle, $\vec{v}$ is the particle velocity, and $\vec{E}$ and $\vec{B}$ are the local electric and magnetic fields, respectively. The charged particles will gyrate around the magnetic fields and the gravitational force and the electric field will cause the charged particles to drift in the $\vec{g} \times \vec{B}$ and $\vec{E} \times \vec{B}$ directions. Near Io, the strongest magnetic field is <2500 nT and therefore, for a singly ionized oxygen atom, the gyration period is ~0.4 s and for an electron the gyration period is ~10^{-5} s. The electron Larmor radius is ~7 m for a typical 5 eV electron and the minimum magnetic field (~1200 nT) expected near Io. This is roughly equal to the mean free path near the surface at the subsolar point (115 K; ~5 m), but much smaller than the atmospheric scale height (>10 km). Everywhere else the electron Larmor radius will be smaller and the mean free path bigger; therefore, resolution of the electron gyro-motion should not be critical. This is fortuitous since timestep resolution of the electron gyration period is currently not feasible for typical atmospheric simulations which require several hours for neutral gas flows to develop and reach a steady state.

While resolution of the exact electron trajectory is not necessary, the electrons must obviously still be moved in space. Therefore, in the current DSMC implementation, the electrons are assumed to move with a given ion for computational ease.[22] For the plasma conditions near Io, with plasma number densities, n_e, from 10^9 m^{-3} (free stream) to 10^{11} m^{-3} (near surface) and electron temperatures less than 5 eV, the Debye length varies from ~0.02 m (near surface) to 0.5 m (free stream). Therefore, the Debye length is everywhere much smaller than the DSMC simulation cell size linked to the mean free path and neutral gas density gradients. While this justifies forcing the electrons to move with the ions in order to preserve quasi-neutrality, it also means our simulation cannot resolve plasma gradients on the Debye length scale in which quasi-neutrality does not hold such as in the near-surface sheath.

When forcing the electrons to move with the ions, the production of an ambipolar electric field due to the electron's higher mobility should be approximated otherwise the effect that the electrons have on the ion motion through the Coulomb force will not be included. From the Boltzmann relation for electrons, derived from the continuum ion and electron momentum equations and noting that the mobility of electrons results in near infinite heat conductivity, one can obtain a relation for the ambipolar electric field, $\vec{E}_{ambi}$:

$$\vec{E}_{ambi} = -\frac{kT_e}{e}\nabla ln(n_e), \tag{2}$$

where k is the Boltzmann constant and T_e is the electron temperature which has been assumed to have negligible gradients.[23] The ambipolar electric field computed from Eq. (2) was superimposed onto the precomputed (externally applied) electric field (see Eq. (3)) obtained by MHD simulations. The assumption that the electron temperature gradients were negligible was necessary from a simulation standpoint since gradients of the temperature would be even noisier than the gradient of the electron density and therefore likely to lead to increased spurious noise in the electric fields. Even with this assumption, the computed ambipolar field was too noisy since the plasma density is less than 0.01% of the neutral density for much of the atmosphere and this noise created simulation difficulties. Therefore, while it was desirable to determine the effect of the plasma flow with ambipolar field, the current simulations do not include this effect. However, the main effect of the ambipolar field should be to twist the local plasma flow across Io as it encounters Io's atmosphere[17] and it should negligibly affect the plasma chemistry. The ambipolar field computation has been smoothed sufficiently by a combination of increased number of simulation particles, time averaging (over thousands of plasma timesteps) the ambipolar field sample, box-car smoothing the sampled electron density, averaging the current $\vec{E}_{ambi}$ computation in each cell with the previous value of $\vec{E}_{ambi}$, and finally box-car smoothing the new averaged value for $\vec{E}_{ambi}$. Future simulations will compare Io's atmosphere including the ambipolar field and the present simulations without the ambipolar field.

The current implementation uses a 3D magnetic field, $\vec{B}$, and bulk plasma velocity, $\vec{v}_{plasma}$, precomputed using a steady state multiscale MHD simulation.[14] The (co-rotational) electric field is computed by taking the cross

product of the plasma bulk velocity and the magnetic field which is then interpolated onto the DSMC grid. As mentioned previously, the electrons are moved with the ions and therefore the total electric field, $\vec{E}$, that affects the charged particles in Eq. (1) is

$$\vec{E} = \vec{E}_{ambi} - \vec{v}_{plasma} \times \vec{B}. \tag{3}$$

While this means that the fields are not self-consistent with the gas dynamics, it gives Io's perturbation of the Jovian field to first order and dramatically reduces the computational cost. The field is sensitive to charged particle noise when solving Maxwell's equations, e.g. a particle crossing into a cell is a current which creates a magnetic field. Hence, a self-consistent simulation of fields would most likely require a particle weighting scheme or implementation of a hybrid DSMC-Particle-In-Cell (PIC) code to determine the fields.[24]

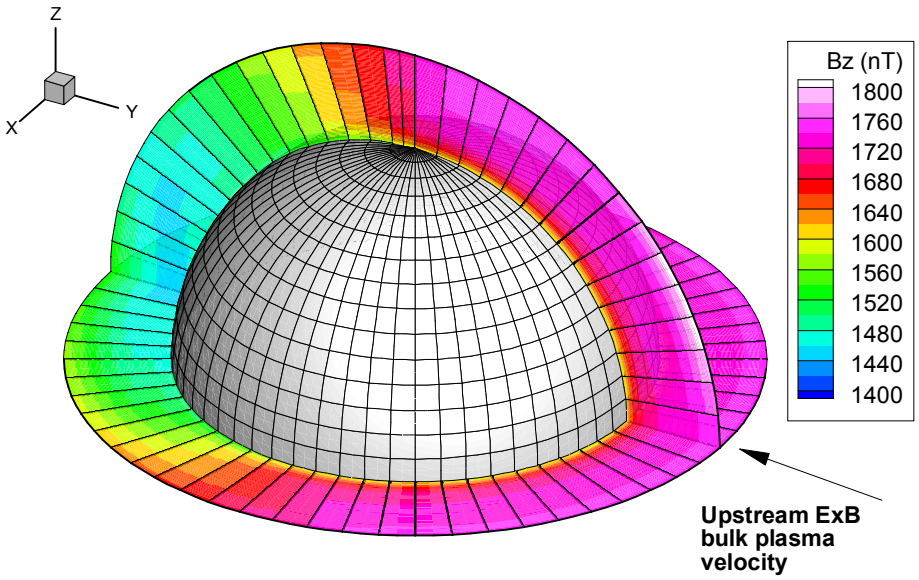

Figure 2. Interpolated magnetic fields across the north pole from the sub- to anti-plasma point and along the equator.

2. Heavy-Heavy Chemistry

DSMC is ideally suited to modeling chemically reacting gas flows due to the molecular nature of the reactions. The molecular dynamics/quasi-classical trajectory (MD/QCT) method can provide accurate cross section data provided the potential energy surfaces of the interacting particles are adequate and quantum effects such as tunneling are not important.[25,26] In our model we will utilize MD/QCT or experimental cross section data when available and linearly interpolate between the data points. If no cross section data are available (MD/QCT or experimental), the total collision energy (TCE) model[27] is used to obtain cross sections that result in continuum rate constants in the modified Arrhenius form. Only reactions for which MD/QCT cross sections or Arrhenius rate coefficients are available are currently modeled. Modeled interaction types include non-reactive inelastic collisions, charge exchange, dissociation, recombination, and radiative recombination. Exchange reactions are neglected (and not implemented) for the current model; in the future they should be included for completeness (e.g. $SO + SO \rightarrow S_2 + O_2$); however, they should be rare and their effect on the global distribution of species should be minor.[28,29] Note that the actual physics of the reaction are identical whether the cross sections are computed via TCE or MD/QCT. The simulations presented here do not include electron-neutral interactions so that the effects of plasma momentum transfer, ion sputtering, and photo and heavy chemistry on the global atmospheric winds and the neutral species distribution can be separated from the effects due to electron chemistry. Since the electron-neutral collisions mainly act to heat and electronically excite the atmosphere (causing aurorae) it is not expected that inclusion of the electron-neutral collisions will change the results shown, except through the ionization of neutrals which then are accelerated by the co-rotational field. Both of these mechanisms will be included in a future work examining their effect on Io's

global atmosphere.

The heavy-heavy reactions included in the model are shown in Table 1 along with the corresponding reference. Note that several of the sulfur reaction cross sections (e.g. $SO_2 + S \rightarrow SO + S + O$) are obtained by scaling the corresponding oxygen reaction cross section (e.g. $SO_2 + O \rightarrow SO + 2O$) so that the two cross sections were the same functions of the total collision energy. In other words, the sulfur reaction cross section as a function of the relative collision velocity for a given reaction, i_{rxn}, is given by

$$\sigma_{S,i_{rxn}}(V_{rel}) = \sigma_{O,i_{rxn}}\left(\sqrt{\frac{m_{r,O}}{m_{r,S}}}V_{rel}\right). \quad (4)$$

Here $m_{r,i}$ is the reduced mass of the particle type i each with the same collision partner (SO_2 in the example reaction above). This was done to extend the available MD/QCT data on energetic $O + SO_2$ collisions to S atoms which comprise one third of the incident plasma. This assumption should be reasonable because at the very high collision energies typical of the jovian plasma sweeping past Io, the cross sections should be mostly independent of the details of the interaction potential surface.

Collision type	Reaction	Reference
Elastic	$SO_2 + O \rightarrow SO_2 + O$	28
Dissociation	$SO_2 + O \rightarrow SO + 2O$	28
Dissociation	$SO_2 + O \rightarrow O_2 + O + S$	28
Dissociation	$SO_2 + O \rightarrow 3O + S$	28
Dissociation	$SO_2 + S \rightarrow SO + O + S$	28†
Dissociation	$SO_2 + S \rightarrow O_2 + 2S$	28†
Dissociation	$SO_2 + S \rightarrow 2O + 2S$	28†
Dissociation	$O_2 + O \rightarrow 3O$	30
Dissociation	$O_2 + S \rightarrow 2O + S$	30†
Charge Exchange	$O^+ + O \rightarrow O + O^+$	31
Charge Exchange	$S^+ + S \rightarrow S + S^+$	31
Radiative Recombination	$SO + O \rightarrow SO_2 + \gamma$	32
Recombination	$O + SO + M \rightarrow SO_2$	5
Recombination	$2O + M \rightarrow O_2 + M$	5
Recombination	$O + S + M \rightarrow SO + M$	5

Table 1. Included Heavy-Heavy Interactions. †Cross section obtained by scaling corresponding SO_2 + O reaction.

We utilize MD/QCT data when they are available for a given reaction in order to account more accurately for internal energy favoring of the reaction rates. A parallel MD/QCT code was developed to calculate reaction and viscosity cross sections at various relative collision velocities and internal energy states for O+HCl collisions.[26] This code was modified to compute reaction and viscosity cross sections for $O+SO_2$ collisions at typical collision energies present within Io's atmosphere.[28] The MD/QCT method simulates an ensemble of individual trajectories through the potential field generated by the molecules. Each trajectory is initialized with a random impact parameter less than b_{max}. After a specified time interval, the post-interaction products, scattering angles, velocities, and internal energy states are examined. One obtains the reaction cross section for a given relative velocity and internal energy from the fraction of trajectories that lead to a specific reaction. Similarly, one can obtain distributions for the post-interaction velocities, internal energies, and scattering angles. While the total collision (scattering) cross section is infinite due to the slow decay of the molecular potential with r, the momentum cross section is finite. Hence, a viscosity based cross section can be computed from the non-reactive trajectory data.[26,28] In general, at low collision velocities (<10 km/s), the VHS model fits the MD/QCT viscosity based cross section data reasonably well. Therefore, for $O+SO_2$ collisions slower than 2 km/s, the non-reactive cross section in our code is computed using the standard VHS model[27] but with parameters set by the curve fit to the MD/QCT viscosity cross section data. For relative collision velocities greater than 2 km/s, the non-reactive cross section is determined directly by linear

interpolation between the available MD/QCT viscosity cross section data points. This is necessary because the VHS curve fit greatly over-estimates the non-reactive cross section above ~20 km/s for O+SO_2 collisions (see Table 1).

Figure 3 shows some of the MD/QCT data (symbols) for O+SO_2 and O+O_2 collisions that are used in the current simulations.[29] Above ~20 km/s the O+SO_2→SO+2O and O+ SO_2→S+3O reactions both exceed the non-reactive MD/QCT cross section. Therefore it is very important to use the total cross section to get the correct collision rate. Note that the O+ SO_2→O_2+S+O reaction cross sections were found to be negligible (<10^{-17} cm^2) by the MD/QCT simulations. While the O_2+O→3O cross section is relatively small, it is an important loss mechanism for O_2 since we currently assume that O_2 is a non-condensable at Io's surface temperatures. Also, the MD/QCT data has large differences in the reaction cross section due to internal energy, especially near threshold total collision energies, that cannot be simply scaled away by renormalizing the cross sections as functions of the total collision energy. Therefore, it is important to simulate the SO_2 internal energy as accurately as possible to get an accurate dissociation rate. Future work will include the MD/QCT post-interaction vibrational and rotational energy state distributions.

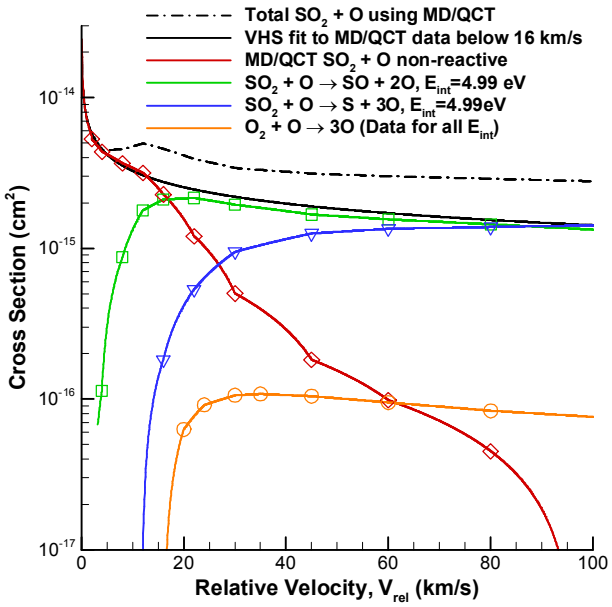

Figure 3. Cross section versus relative velocity for several included reactions. Between the MD/QCT data points (symbols) the cross section is obtained via linear interpolation (curved lines on the log plot) in both relative velocity and internal energy (see dashed black line).

Besides the heavy neutral chemistry described above, the current model includes resonant charge exchange reactions in which a charged atom or molecule exchanges an electron with a neutral atom or molecule of the same species. Non-resonant charge exchange was neglected in the current work since the resonant charge exchange cross section is typically 100 times greater than the non-resonant cross section. However, around the subsolar point, near the surface of Io, it is likely that non-resonant charge exchange is non-negligible since the SO_2 density exceeds the primary charged particle (O and S) densities by more than 100 times.

In a resonant charge exchange interaction, only the electron is transferred and since its mass is negligible compared to the atom or molecule, the momentum and energy of the two interacting particles are unchanged by the interaction. During resonant charge exchange, the (typically slow) neutral becomes a positive ion which then re-accelerates due to the external fields and the (typically fast) ion becomes a neutral, unattached to the field lines. Theoretical resonant charge exchange cross sections for many elements have been tabulated at relative energies of 0.1, 1, and 10 eV and the data for O and S were used to fit the parameters in the theoretical equation for resonant charge exchange in order to extend the cross section data to the higher energies of interest for Io

$$\sigma(V_{rel}) = \frac{\pi}{2\gamma^2} ln^2 \left(\frac{v_o}{V_{rel}}\right), \tag{5}$$

where V_{rel} is the relative velocity between the ion and the neutral atoms and γ and v_0 are constants for a given atom.[31]

Equation (5) was used to generate resonant charge exchange cross sections at 10 (arbitrary) relative energies. These were then used as input for the DSMC simulations. Figure 4 shows the analytic (solid black lines, Eq. (5)) and DSMC resonant charge exchange cross sections (red curves) versus relative velocity for the O^+ and S^+ ions as well as the original charge exchange cross section data ("X" symbols). Note that the DSMC cross sections are linearly interpolated between the set of "data points" obtained from Eq. (5), and that above 125 km/s (the last data point), the slope between the two previous cross sections is used to extend the cross section. However, very few ions will have velocities greater than 100 km/s and therefore the small error due to linear extrapolation is acceptable and it was not deemed necessary to add another data point.

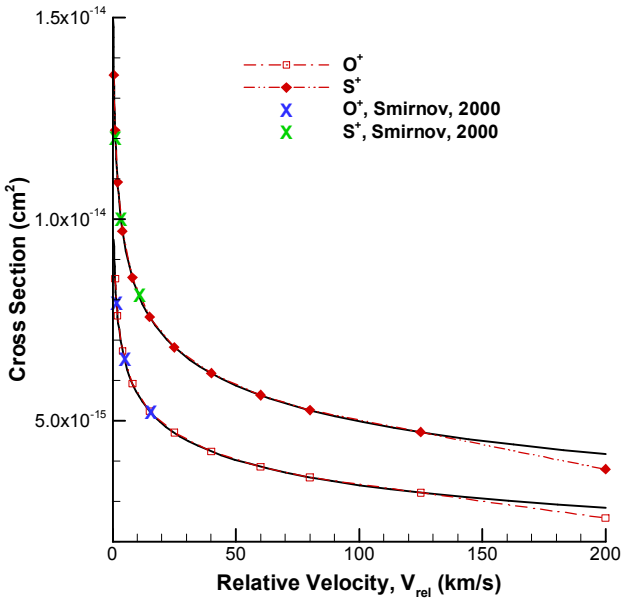

Figure 4. Resonant charge exchange cross sections versus relative velocity.

B. Surface Sputtering Model

For Io, sputtering of surface frost via energetic ion impact is important when the atmospheric column density falls below ~10^{16} cm^{-2}.[33,34] Assuming non-negligible local frost coverage, this occurs locally when the surface frost temperature falls below ~109 K. Since the surface frost temperature drops below 90 K near the poles and below 109 K on the nightside, direct surface sputtering will occur over large regions of Io's surface. Consequently, an atmospheric column forms that is greater than that due to sublimation alone. Furthermore, the reduction in the subsolar–polar and subsolar–nightside pressure gradient should affect the strength of the circumplanetary winds. Since auroral limb glow emission is observed at the poles, inclusion of surface sputtering should be important.

Laboratory data are lacking for surface sputtering of SO_2 frost via oxygen and sulfur ions at energies typical for the jovian thermal plasma torus (<0.6 keV). A non-thermal energetic component of ions is present at Io and, while the sputtering yield per incident ion is much higher at larger energies, the flux incident to the surface is much smaller than the co-rotating thermal ions. Accounting for both effects, the overall sputtering yield of the energetic ions is an order of magnitude less than for the co-rotating ions.[35] Hence, sputtering due to energetic ions is ignored in the present work. Unfortunately, laboratory data are only available at incident ion energies greater than 10 keV and are from the 1980s, presumably motivated by Voyager 1 observations.[34,36-38]

If an ion hits the frost covered surface during the move step in the planetary DSMC code, the total sputtering yield is determined based on the ion and frost species and the incident ion energy. Next, the number sputtered and the incident ion energy are stored along with the location for each ion that impacts the surface. Then, at the start of the next time step, the sputtered particles for each ion impact are created and given a translational energy based on the Thompson collisional cascade energy distribution. The velocity vector is picked assuming an isotropic angular distribution away from the surface. The molecules are given an internal energy based on equilibrium with the local surface temperature. This is almost certainly too "cold" of a distribution, but any error in the species' densities (the

primary quantity of interest) caused by this approximation is negligible compared with the errors in determining the total and fractional yields.

Another issue is that DSMC has difficulty handling the fact that a sputtering event is (nearly) a point source of molecules expanding away from each other. The problem is that, for small enough time steps, the sputtered molecules remain in the same cell (which is much larger than the sputtered area) and are then likely to be selected for collision with each other, because they have large relative velocities with each other (see Figure 5). The center of mass velocity of the sputtered particles is normal to the point of impact on the surface (excluding noise); however, collisions between particles streaming away from each other will tend to reduce the expansion velocity parallel to the surface. Consequently, unphysical collisions between sputtered particles lead to the formation of a vertical jet of particles instead of an expanding cloud.

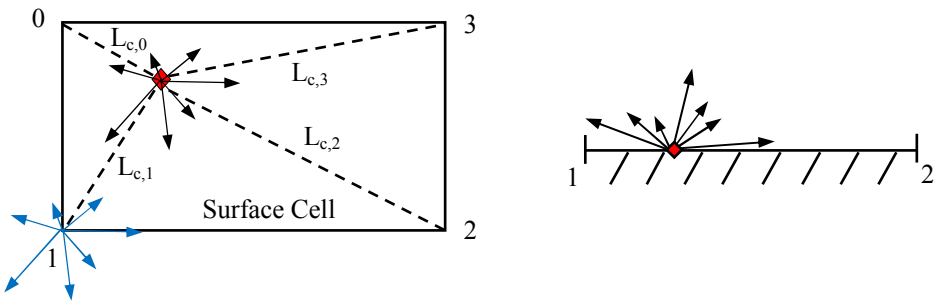

Figure 5. Schematic of sputtered particle placement to the surface cell corners from an ion surface impact located at the red diamond. Left: Top view of the surface cell. Right: Side view of the cell. The velocity vectors for seven sputtered particles are shown at the impact point (black) and at the (randomly determined) particle's creation corner (blue). The distance from the cell corners are given by dashed black lines.

A "sputtered" identifier flag on the molecule structure to prevent collisions would both add memory overhead and add computational cost during the collision routine. To reduce the error, all of the sputtered particles are placed at a surface cell corner with the probability that the i^{th} corner is picked inversely proportional to the distance of the sputter event from that cell corner

$$P_{sput,i} = \frac{1/L_{c,i}}{\sum_{j=0}^{3} 1/L_{c,j}}, \tag{6}$$

where $L_{c,i}$ is the distance from the sputter location to the i^{th} corner (see Figure 5). If an ion impacts exactly on a corner, then all of the sputtered particles are placed at the corner. As seen in Figure 5, putting the sputtered particles at a cell corner instead of the ion impact point reduces the likelihood that two particles which are moving away from each other remain in the same cell, and hence reduces the probability of collisions between them. This does introduce errors linked to the cell size and, over many impacts, smears the sputtered particles over the cell area. The smearing, which is at the spatial resolution limit of the computation, was deemed preferable to forming unphysical jets of particles streaming radially away from the surface.

3. Sputtering Yield

Once an ion hits the SO_2 frost surface, the first step is to determine the number of sputtered particles. Since SO_2 sputtering data are available only for much higher incident ion energies (>10 keV) than the energy of oxygen and sulfur ions in the co-rotating torus, the yields measured at high energy must be extrapolated to the relatively low torus energies. [34,38] The physical mechanism for low energy sputtering is given in detail in Ref. 39; the specific model used is described below.

Assuming that each recoil atom interacts independently with the other surface atoms, a collisional cascade of momentum and energy transfer between the recoil atoms and the surface atoms occurs and any of the independent collision cascades near the surface can result in surface particles being sputtered. If the diffusion cross section is independent of the incident ion species, then the sputtering yield due to the collision cascade at low incident ion energies is linearly proportional to the incident ion energy, E_i, with a constant, $C_{A,B}$, dependent on the ion species, A, and the surface species, B:

$$Y_{A,B} = C_{A,B}\alpha_{A,B}\gamma E_i;\ \ \gamma = \frac{4m_A m_B}{(m_A+m_B)^2} \tag{7}$$

where the fraction, $\alpha_{A,B}$, of the energy deposited which does not contribute to sputtering has been experimentally measured for various ions and surfaces. Within the accuracy of the model, $\alpha_{A,B}$ is found to be only a function of m_A/m_B.[40] The collision cascade sputtering yield is seen to be linear in the ion impact energy and the constant $C_{A,B}$ is determined by linearly fitting to the available sputtering yield data. Unfortunately, the measured sputtering yields are not fully in the collision cascade regime even at the lowest incident ion energies and the electronic sputtering component (sputtering due to electronic excitation) is non-negligible. The sputtering yield for O^+ and S^+ at their respective corotational energies (dominated by collision cascade sputtering) have been estimated by subtracting an estimated electronic sputtering component from the total measured yield to get the collision cascade component at the lab ion energies and then extrapolating the collision cascade sputtering yields to the appropriate corotational plasma energies.[41,42] Due to collisions with Io's atmosphere, the ions impacting the surface will, in general, have a distribution of energies. Therefore, the sputtering yield (Eq. (7)) is determined using a linear fit to the O^+ and S^+ sputtering yields at corotational energies normalized by $\alpha_{A,B}\gamma$, as shown by the solid black line in Figure 6.[41,42] The sputtering yields for a given incident ion are then computed by multiplying the normalized sputtering yield, $Y_{A,B}/(\alpha_{A,B}\gamma)$, by the appropriate value of $\alpha_{A,B}\gamma$, as shown for O^+ ions (red dashed line) and S^+ ions (blue dot-dashed line) in Figure 6.

Note that the linear curve fit for the sputtered yield in Figure 6 is not equal to zero when an ion impacts the surface with zero energy. Obviously, this is not physical since the model assumes $E_i \gg U_b$ and at very low incident ion energies this condition does not hold and the model breaks down. A threshold for sputtering occurs when the maximum energy transfer is of order the surface binding energy and the collisional cascade model fails. The threshold energy, E_t, has been experimentally investigated and E_t/U_b is primarily a function of m_B/m_A.[39] For sputtering of SO_2 frost by the ions of interest here, $E_t/U_b \leq 10$ and the binding energy, U_b, is roughly equivalent to the sublimation energy which, for SO_2, is 0.357 eV.[38] However, due to energy distribution constraints discussed below, it is found to be computationally desirable in the current model to set the sputtering yield to zero below $20U_b = 7.14$ eV.

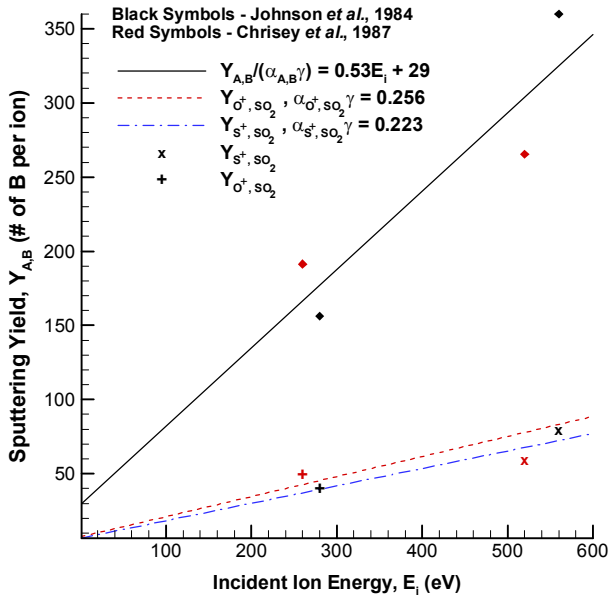

Figure 6. Curve fit sputtering yield versus incident ion energy. The black solid line and diamond symbols are actually the sputtering yield normalized by $\alpha_{A,B}\gamma$, the dashed and dot-dashed lines and the '+' and 'x' symbols give the sputtering yields for O^+ and S^+ ions incident onto SO_2 frost.

As the SO_2 frost temperature, T_s, increases, one might expect the sputtering yield for a given incident ion energy to increase. The sputtering yield as a function of surface temperature for condensed gas solids, including SO_2, has been examined, and the sputtering yield does indeed increase with increasing surface temperature above a threshold

temperature.[43] For 1.5 MeV He^+ ions incident onto SO_2 frost, the sputtering yield is constant until a frost temperature of ~60 K, above which the yield increases exponentially in the form:

$$Y = Y_0 + Y_1 exp(-\Delta E/kT_s), \tag{8}$$

where Y_0, Y_1, and ΔE are parameters set by curve-fitting the data.[34] While the sputtering yield due to the He^+ ions is dominated by electronic deposition, in the current model it is assumed, for lack of any other data, that the increase in sputtering yield with surface temperature is similar at the vastly lower incident ion energies of present interest.[44] The exponential increase in SO_2 sputtering with increasing surface temperature has been attributed to two mechanisms based on analogy to experiments with sputtering of D_2O ice.[37] The initial (small) increase in sputtering yield is due to increased production of SO_2 products: SO, O_2, and SO_3. Above a threshold temperature the yield increases because energy that does not go into sputtering a particle locally heats the solid and increases the local sublimation rate. This threshold temperature is not precisely known because there are no data available on product-production as a function of surface temperature for SO_2.

Incident corotational ions have energies of several hundred eV and can, in theory, readily dissociate the SO_2 frost. However, lower energy ions impacting the surface might be much less effective at sputtering SO_2 daughter species since dissociating the SO_2 would take up a significant fraction of the ion energy. It was found that, for 45 keV incident Ar^+ ions, ~10% of the sputter particles were SO and at most several percent were SO_3 or S_2O.[41] However, as noted earlier, the increased sputtering with increasing surface temperature is attributed first to increased chemical activity and then to increased local sublimation.[37] It is therefore unclear what fraction of the sputtered particles should be daughter products of SO_2 at a given surface temperature and incident ion energy. The current model neglects sputtering of species other than the parent frost species since the fraction of sputter daughter products is relatively low for 45 keV Ar^+ ions incident on 15 K SO_2 frost and would arguably be even lower for <0.5 keV O^+ and S^+ ions incident on >90 K SO_2 frost.

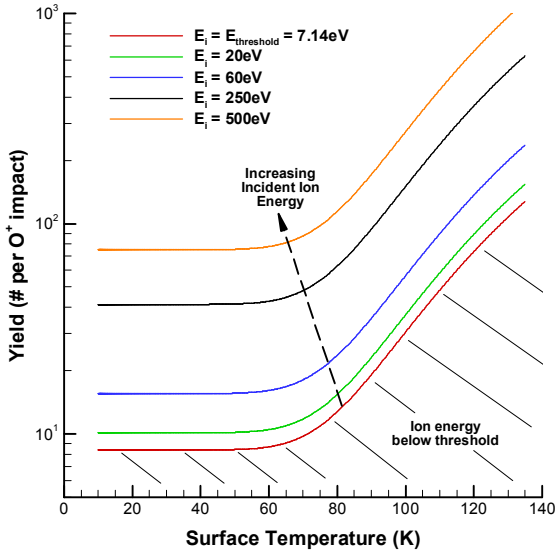

Figure 7. Simulation sputtering yield versus surface frost temperature at several O^+ ion energies. Note that S^+ ion yield curves would be similar in shape, displaced slightly due to the $\alpha_{A,B}\gamma$ factor. Note that at very high temperatures the yield asymptotes to $1 + Y_1/Y_2$ times the low temperature yield, see Eq. (9).

To account for the both the sputter yield dependence on incident ion energy and the surface temperature, the total number of sputtered particles in the current model is given by

$$Y_{A,B} = floor\left(\frac{Y_{A,B}}{(\alpha_{A,B\gamma})} \times \alpha_{A,B\gamma} \times \left[1 + \frac{Y_1}{Y_0} exp(-\Delta E/kT_s)\right] + R\right), \tag{9}$$

where the *floor*() is taken and a random number, R, added since $Y_{A,B}$ must be an integer. $Y_{A,B}/(\alpha_{A,B}\gamma)$ is given by curve

fit (Figure 6) to be $Y_{A,B}/(\alpha_{A,B}\gamma) = 0.53E_i + 29$, $\alpha_{A,B}\gamma$ is determined based on the ion species and Figure 3.17 in Johnson.[39] Y_0, Y_1, and ΔE (16, 2.8×10^4, and 0.056 eV respectively) are given by curve fit.[34] The yield as a function of surface temperature given by Eq. (9) is shown in Figure 7 for O^+ ions hitting SO_2 frost at several incident ion energies above the threshold energy (7.14 eV). Io's peak surface frost temperature is ~115 K and an energetic O^+ ion incident onto the surface would yield ~500 SO_2 molecule, but the sublimation atmosphere present above 115 K SO_2 frost should be sufficient to prevent such high energy ions from reaching the surface. However, the sensitivity of both sublimation and sputtering yield to the surface temperature could conceivably result in sharp density gradients as the surface temperature drops towards the poles (and terminators), as inferred from Lyman-α observations.[45,46]

4. Sputtered Particle Energy Distribution

For a given ion impacting the surface, knowing the number of sputtered particles is, by itself, insufficient to model the sputtered atmosphere. At the least, a kinetic energy distribution for the sputtered particles must be prescribed and, if the particles are molecules, internal energy distributions must be given. Again, the co-rotating ions are in the low energy regime and therefore impacts should result in limited electronic excitation of the surface particles. Therefore, the kinetic energy distribution, f_E, is reasonably described by the Thompson distribution derived using the collisional cascade model:

$$f_E(E_s) = \frac{C_E(E_s,\theta_i)E_s}{(E_s+E_b)^3}, \tag{10}$$

where E_s is the sputtered particle energy, E_b is the effective binding energy of the surface (different from U_b), and $C_E(E_s,\theta_i)$ is a proportionality constant estimated from experimental data.[40] In the current model, the proportionality constant is set to $C_E(E_s,\theta_i) = 2E_b$ based on the experimental yield.[47,48] Experiments have shown excellent agreement between the experimental sputtered particle energy distribution and the collisional cascade energy distribution.[38] For 45 keV Ar^+ ions incident onto 15 K SO_2 frost, the experimental data was best fit by an effective binding energy, E_b, of 0.054 eV. Note that the Thompson distribution is independent of the incident ion energy since in the collision cascade model the particles which sputter off the surface are, in general, given the energy to leave the surface not by the initial ion momentum transfer, but by successive collisions with the other particles in the solid.

The current model draws each sputtered particle's kinetic energy from Eq. (10) and draws its internal energies from equilibrium distributions at the local surface temperature. To draw the kinetic energy from the Thompson energy distribution the distribution is integrated to give the cumulative distribution function, $F_E(E_s)$, from [0,1]:

$$F_E(E_s) = 1 - \frac{E_b(E_b+2E_s)}{(E_b+E_s)^2}. \tag{11}$$

The cumulative distribution is then inverted giving $E_s(F_E)$ and, replacing F_E with a random number draw, $R = (0,1]$, the sputtered particle energy is given by:

$$\mathrm{E_s} = \frac{\sqrt{\mathrm{R}}}{1-\sqrt{\mathrm{R}}}\mathrm{E_b}. \tag{12}$$

Note that drawing the sputtered particle energies from Eq. (12) could result in the sum of the sputtered particle energies exceeding the incident ion energy because there is no dependence in Eq. (12) on the incident ion energy. While the probability that this occurs is very small for most incident ion energies and surface temperatures, it does occur more frequently for near-threshold ion energies when the surface temperature is high (~115 K). One can attempt to force energy conservation for a given sputtering event with $Y_{A,B}$ sputtered particles by enforcing a maximum energy for the j^{th} particle's energy given by energy conservation. However, this was found to undesirably distort the distribution and artificially increase the number of particles given very low energies due to the rare high energy sputtering event (that uses most of the incident ion energy) occurring for one of the first particles generated.[49] Therefore the current model ignores the lack of energy conservation and instead assumes that any excess energy required is provided by the surface. The surface cooling due to this effect was found to be minor.

C. Photo-Chemistry Model

Photo-chemistry has been shown to be an important mechanism for production of the minor dayside species (SO,

O_2, S, and O) from sublimated SO_2 gas.[50] Furthermore, Austin and Goldstein showed that circumplanetary winds transported dayside species onto the nightside and therefore it is necessary to properly account for the photo-chemistry of the initial quasi-steady atmosphere.[51] For the current work, the photo-chemistry model assumes the gas to be optically thin, but now when a photo-dissociation or photo-ionization event occurs, the simulation particle is broken into the appropriate products for the specific photo-reaction and the total number of simulation particles is increased.[49] Furthermore, reflected light from the surface is not included in the model; generally the photo-reaction cross sections are small at the longer wavelengths (>4000 Å) where the surface reflectance of Io is significant.[52] If the initial simulation particle is a molecule, then any internal energy of that molecule is assumed to go into the relative translational motion of the products and any molecular products are assumed to have no internal energy upon creation. Furthermore, the current model assumes that the products can simply be given an additional mean excess energy upon dissociation or ionization.[49,53] Table 2 shows the included photo-reactions and the associated rates and excess energies.

Reaction	Rate Coefficient‡ (s^{-1})	Excess Energy (eV)
$SO_2 + h\nu \rightarrow SO + O$	5.9×10^{-6}	0.44
$SO_2 + h\nu \rightarrow O_2 + S$	1.9×10^{-6}	0.75
$SO_2 + h\nu \rightarrow SO_2^+ + e^-$	3.9×10^{-8}	12.0
$SO + h\nu \rightarrow S + O$	2.3×10^{-5}	0.62
$SO + h\nu \rightarrow SO^+ + e^-$	3.2×10^{-8}	8.62
$O_2 + h\nu \rightarrow 2O$	1.6×10^{-8}	1.48
$O_2 + h\nu \rightarrow O_2^+ + e^-$	1.7×10^{-8}	19.30
$S + h\nu \rightarrow S^+ + e^-$	4.0×10^{-8}	6.30
$O + h\nu \rightarrow O^+ + e^-$	7.8×10^{-9}	21.60

Table 2. Summary of included photo-reactions assuming a Sun-Jupiter distance of 5.2 AU. ‡Rate coefficients from Ref. 53.

III. Results

The planetary DSMC code described in the previous section has been used to simulate a multi-species atmosphere on Io. The present 3D DSMC simulations of Io's sublimation and sputtered atmosphere includes the effects of photo-chemistry, sputtering, and realistic plasma interaction (momentum transfer, heating, and chemistry) on the dynamics of Io's global atmosphere.

For computational simplicity, the present simulations assume that Io's surface is covered uniformly by SO_2 frost and that the surface temperature is in instantaneous radiative equilibrium with insolation. These surface boundary conditions have been used in past simulations of Io's atmosphere.[51,54] Furthermore, while this surface model does not represent the actual Ionian conditions, in order to understand the more complicated atmosphere that will result from non-uniform frost and more accurate surface temperature distributions, it is useful to first examine the simpler atmosphere simulated here. Both of these approximations have been improved upon by Walker *et al.* which used a surface frost map and a two temperature frost/non-frost surface model that accounted for Io's rotation in order to simulate a pure SO_2 sublimation atmosphere.[55,56] However, these prior simulations used a radial plasma heating model with no plasma-neutral momentum transfer or chemistry.[51,55] The uniform frost assumption should have little effect on the global atmospheric structure and winds; non-uniform frost seems to have little effect on the overall atmosphere, except in the formation of a dawn atmospheric enhancement in the column density which depended upon the residence time of SO_2 molecules on the non-frost surface.[55] While the frost was not in instantaneous radiative equilibrium with insolation due to Io's rotation, the principal effect was to shift the frost temperature distribution longitudinally relative to the instantaneous radiative equilibrium distribution. More recent simulations have found that, for the predicted frost thermal inertias, the frost temperature distribution forms a latitudinal warm "band" shape centered at the equator; this is unlike the "bulls-eye" shape that results from instantaneous radiative equilibrium.[57] The atmospheric dynamics will certainly change depending on the surface temperature distribution; but for the current work it was computationally necessary to assume Io's frost surface was in radiative equilibrium. Future work will simulate the atmospheric response upon entry into eclipse and incorporate our sophisticated dual-

surface temperature model.[57]

The following simulation examines the steady state atmosphere developed on Io due to sublimation, sputtering, plasma flow past Io, and photo- and plasma-chemistry just before eclipse. For the present simulations, the Galileo J0 flyby upstream plasma conditions (plasma density of 3600 cm^{-3}, electron temperature of 5 eV, and ion temperature of 100 eV) are used as well as Ref. 14's simulated MHD magnetic field data which used parameters so that their results best-fit the J0 magnetic field data. The present simulation models the O^+ and S^+ plasma flow past Io and the resultant atmospheric dynamics, modeling the SO_2, SO, O_2, O, S, SO_2^+, SO+, O_2^+, O^+, S^+. Note that in the current model it has been assumed that the condensable species are lost when incident onto the surface. However, in reality the particles should reside on the surface for some time and eventually gain enough energy to leave the surface, possibly after undergoing surface chemistry with another surface-bound particle (and in the case of ions, neutralizing). While this production mechanism is not modeled, it is expected that the O and S atoms on the surface predominately undergo surface chemistry and then leave the surface as SO_2, O_2, or possibly SO (allotropes of sulfur, S_2, S_4, S_8, etc. are expected to remain on the surface). If more SO_2 is formed in this way it would merely add to the frost layer and sublimate (or sputter) from the surface in the same way as current frost model. However, since the current simulation assumes an infinite, uniform reservoir of SO_2 frost adding SO_2 to the frost layer will have no effect on the sublimation rate. The O_2 or SO created on the surface which then sublimates away could very well matter for the near surface gas density, especially on the nightside, and should be examined in future work.

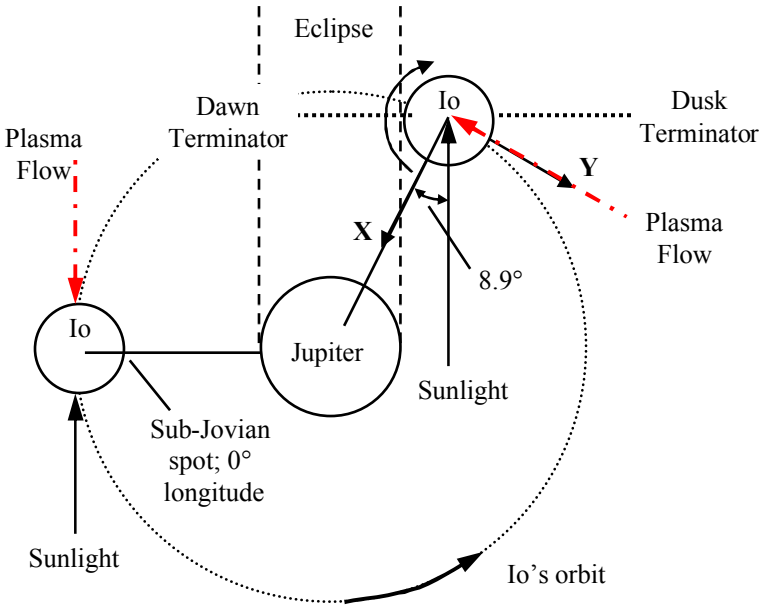

Figure 8. Schematic of Io's location in the Jovian system for the current simulations (not to scale). The DSMC simulation's X (sub-jovian) and Y (sub-plasma) axis (see axis insets in the 3D plots) as well as the direction of increasing longitude are shown to orient the simulation results.

Figure 8 shows a schematic of Io's position in the Jovian system for the current simulations just prior to ingress into eclipse. Io and the bulk plasma rotate counter-clockwise about Jupiter, however, the plasma velocity is ~57 km/s greater than Io's orbital speed and it overtakes Io's trailing[§§] hemisphere with the sub-plasma point at 270° longitude. Note that the subsolar longitude is 351.1° just prior to eclipse, the effect of which is seen in the surface temperature contours shown in Figure 9. The surface temperature, T_S, is given by:

$$T_S(\theta) = \begin{cases} 30cos^{0.25}(\theta) + T_{s,min} & \theta < 90° \\ T_{s,min} & \theta \geq 90°, \end{cases} \quad (13)$$

where $T_{s,min}$ is the nightside temperature which was set to 90 K, and θ is the subsolar zenith angle.

[§§] The leading hemisphere refers to the hemisphere which faces the direction of Io's orbit.

The current simulation solves for the atmosphere in the northern hemisphere of Io with collision cells that extend to 800 km altitude and a free molecular buffer cell that extends the domain to one Io-radius above the surface (1820 km). It is assumed that the plasma flow is symmetric about Io's equator. Four hundred radial collision cells which radially stretch during the simulation, adapting to the local mean free path, are used. The resulting grid is mean free path resolved in the radial dimension over most of the surface; regions of the surface above ~113 K have large enough near surface densities that the radial cells are not quite mean free path resolved. However, the radial density gradients are easily resolved. On the other hand, the latitudinal and longitudinal grid are currently not well resolved, using 3°×3° cells. This was done for efficiency and so that an adequate number of plasma particles would be simulated in each column given that the gas is weakly ionized over much of the domain. However, appreciable differences were not observed between the current simulations and a separate 6°×6° latitude/longitude cell size simulation (not presented). The computation was approximately load balanced by adaptively weighting simulation particles such that each column contains the same number (currently 4×10^4) of simulation particles averaged over many timesteps.

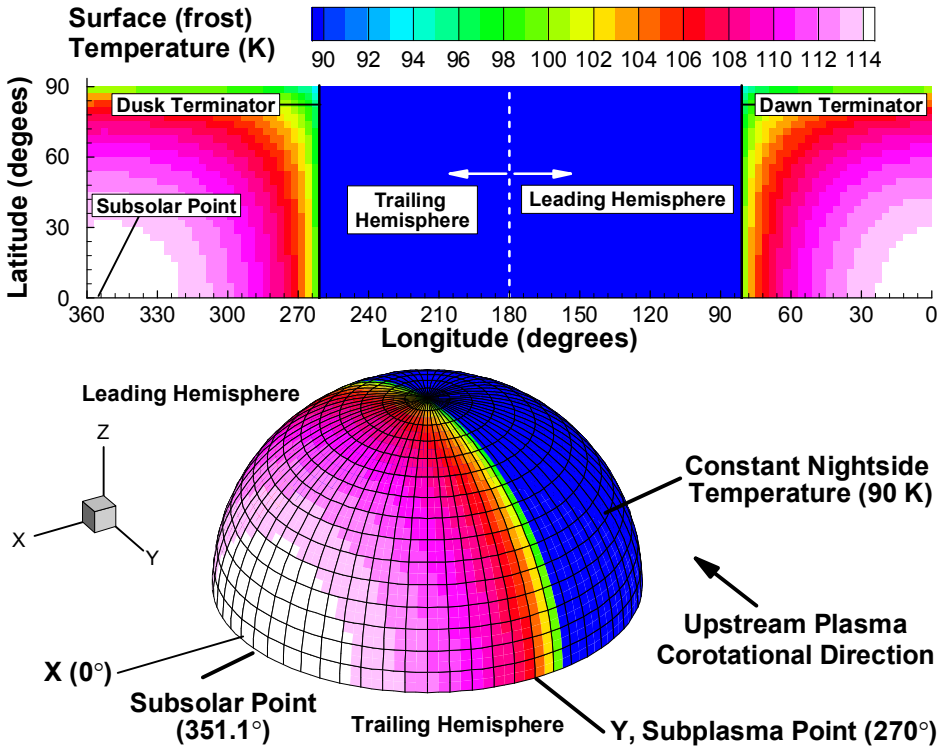

Figure 9. Contours of the initial dayside surface (frost) temperature before ingress into eclipse as a function of latitude and longitude. The subsolar point is at a longitude of 351.1°. The 3D perspective view shows the processor decomposition (900 cpu's, black mesh) and the temperature variation on the trailing hemisphere; the upstream bulk plasma velocity is along the Y-axis.

D. Steady State Atmosphere: Overall Flow Features

As in prior models[51,54,55], circumplanetary flow develops from the high vapor pressure region near the subsolar point to the low vapor pressure nightside. However, now the flow is complicated by momentum flux from the plasma flowing past Io. To examine the overall flow features, near surface (4 km altitude, for comparison to Ref. 55) contours of several representative species (SO_2, O_2, O, and O^+) densities and their respective streamlines are shown in the following figures. The current simulations are truly steady because the surface temperature and sub-plasma point are not changing. Therefore, the following plots (Figures 11 and 12) show 20 minute time averages of the simulation after 8 hours of simulation time to improve the statistics. The top panel shows the trailing hemisphere (the same viewpoint as in Figure 9) and the bottom panel shows the leading hemisphere (the viewpoint rotated 180° from the top panel). The properties over the last few simulation hours changed very little so the following results are

at least in quasi-steady state.

Note that streamlines in a collisionless flow[***], like those above the exobase (~100 km on the dayside), can be deceptive. For example, if two collisionless particle streams with nearly opposite velocities cross in a cell, the resultant bulk sampled velocity in the DSMC cells is nearly horizontal. A streamline drawn using the bulk velocity would show the flow going from left to right, and, while not incorrect, the actual pathlines (particle trajectories) would obviously not follow the streamline. Streamlines are still useful to interpret the flow where the gas is collisional (near the surface on the dayside), and may be useful even when the gas is rarefied (such as the O^+ streamlines which follow field lines) as they still show the net gas flux.

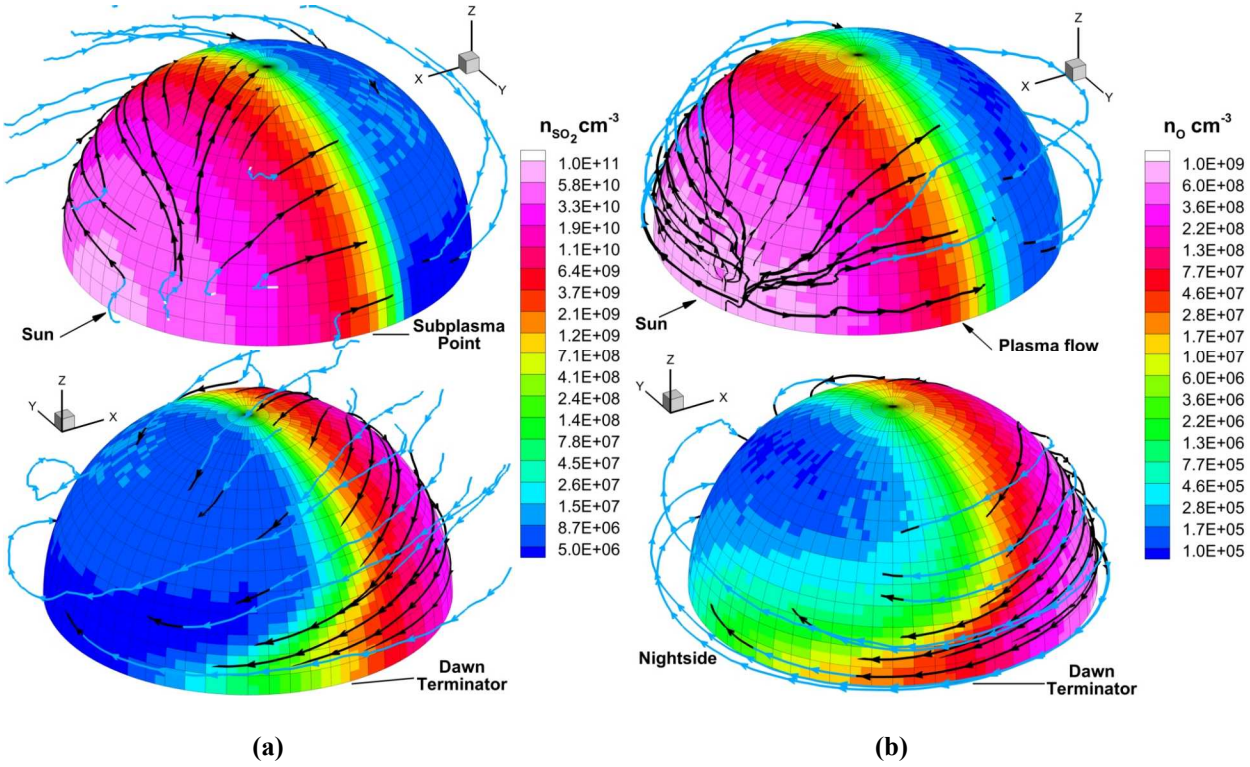

Figure 10. Color contours of (a) the SO_2 density and (b) the O density 4 km above the surface on the trailing (top) and leading (bottom) hemispheres. Solid lines with arrows are streamlines; above 100 km altitude they are light blue, below they are black. The upstream plasma flows inward along the Y-axis.

The near-surface SO_2 number density on both the trailing (top) and leading (bottom) hemispheres is shown in Figure 10a. The SO_2 number density is seen to peak (as expected) in the subsolar region where the sublimation rate is greatest and falls off sharply at the terminator due to the steep surface temperature gradient in the current surface model. Similar to prior models, the near surface SO_2 streamlines (black) show a flow predominantly from the dense dayside region towards the cold nightside. The streamlines do not appear to originate from the subsolar point region (Figure 10a, top), probably because the SO_2 pressure (not shown) at 4 km altitude peaks several degrees from the subsolar point in the direction of the subplasma point; this is likely due to plasma heating. Unlike the near surface flow towards the dusk terminator, the near surface flow from the leading hemisphere in the equatorial region travels far onto the nightside across the dawn terminator. For Io's orbital location in this simulation, the field lines are sweeping past Io from the dusk to dawn terminators and the ions which travel on the field lines transfer momentum (roughly) in the negative Y-axis direction (see Figure 9) because of this. Additionally, the ion motion along the field lines transfers momentum in the Z-axis direction towards the equator because ions that reach Io's surface are assumed lost (see O^+ streamlines in Figure 12b). The result is that the atmospheric winds on the leading hemisphere extend much further onto the nightside than the trailing hemisphere winds do. The resultant retrograde winds disagree with the observations of prograde winds; however, their observations were of Io at eastern and western

[***] Really just a collection of ballistic particle trajectories.

elongation when the subplasma point is at the antisolar and subsolar point respectively.[58] Also, the current simulation surface temperature distribution does not include a surface thermal inertia and it assumes the subsolar point is at a constant longitude. Note that these effects change the overall wind dynamics a great deal therefore the current simulations are not to be considered comprehensive simulations of Io's atmosphere.[55,57]

High altitude streamlines, which might be deceptive, show SO_2 flows around Io from the leading hemisphere dayside (Figure 10a, top image) to the trailing hemisphere's nightside (bottom image) where it then abruptly turns towards the surface as it encounters the plasma flow (however this might not correspond to particle paths). It is possible that this is exactly the situation described earlier, with two streams of particles passing through one another resulting in a deceptive streamline. However, since these are SO_2 streamlines the counter-flowing stream would have to be SO_2 also and there is no evidence of such a flow. Instead it seems more likely that the nearly orbital SO_2 flow encounters the plasma flowing in the opposite direction and then "slowly" collides with it over several hundred kilometers until the SO_2 falls to the surface. Finally, note that the blue streamlines on the upper left of the top image in Figure 10a are ending at the edge of the output grid (though the free molecular buffer cell extends another 1020 km).

Figure 10b shows the near surface atomic oxygen density along with the O velocity streamlines. The oxygen density is highest on the dayside since the parent species densities (SO_2, SO, O_2) are highest on the dayside and O is condensable on the nightside. However, this might also indicate that photo-dissociation dominates plasma impact as a production mechanism, as found in prior simulations.[59,60] Again, the day-to-night flow of oxygen on the trailing hemisphere is found to stop near the dusk terminator and high altitude "flows" originate from streamlines starting ~20° from the subsolar point. These high altitude streamlines are seen to flow most of the way around Io until meeting the plasma flow on the trailing hemisphere. Finally, similar to SO_2, there is a clear buildup of oxygen on the leading hemisphere's nightside as the circumplanetary flow streams away from the northern latitudes due to momentum transfer from the plasma and increased nightside pressures at latitudes due to sputtering. The nightside is collisionless over atmospheric scale height length scales; however, the length scales for the streamline curvature are significantly larger indicating that the nightside pressure distribution affects the curvature of the streamlines.

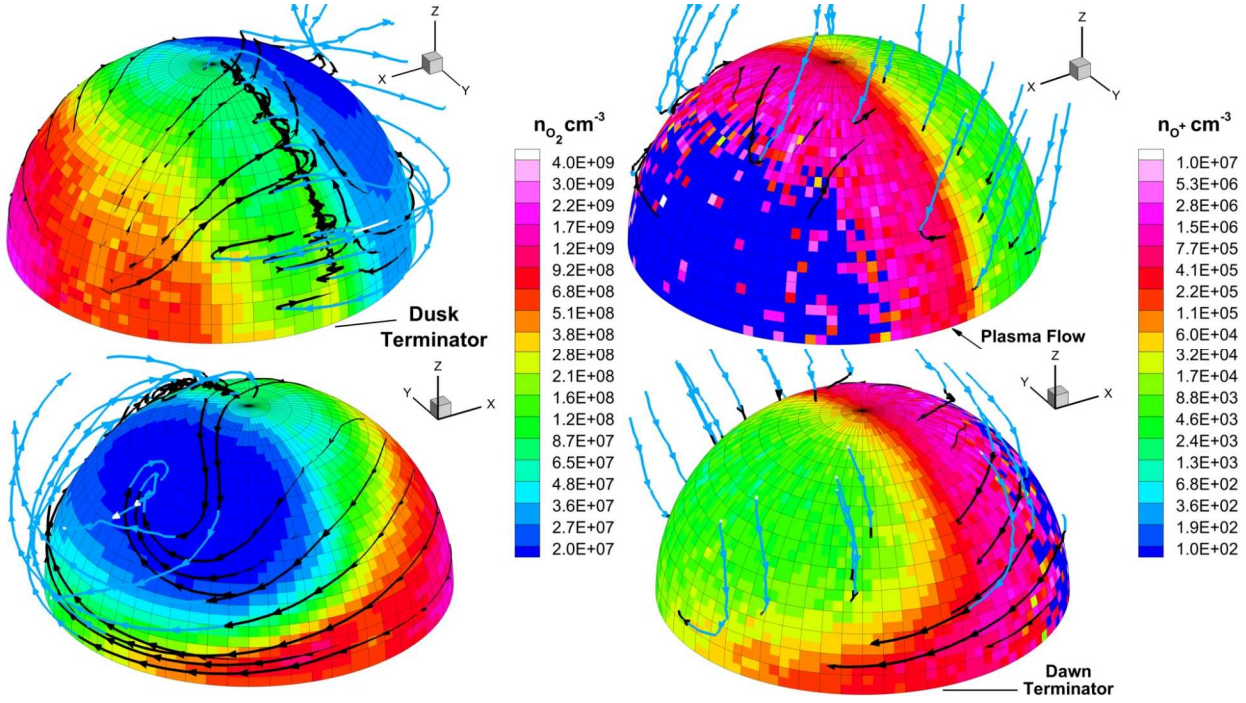

Figure 11. Color contours of the (a) O_2 density and (b) O^+ density 4 km above the surface on the trailing (top) and leading (bottom) hemispheres. Solid lines with arrows are streamlines; above 100 km altitude they are light blue, below they are black. The upstream plasma flows inward along the Y-axis. The upstream plasma flows inward along the Y-axis and has an O^+ density of 2400 cm^{-3}. Note that the abrupt change on the dayside (from pink to blue in one cell) is partly due to insufficient ion particle statistics on the dayside and grid resolution.

The O_2 near-surface density and streamlines are shown in Figure 11a. There are striking differences from the previous two species because, in the current model, O_2 is non-condensable. It is seen that the O_2 density is highest on the dayside where is formed via photo-dissociation of SO_2 (the plasma-dissociation cross section is negligible). However, the density variation from dayside to nightside is much less (only ~100×) than for the condensable species, as expected. Thus the logarithmic color scale on this figure only extends over roughly two orders of magnitude instead of four or five orders of magnitude in the two previous figures. This leads to the nightside high density region near the equator extending from the dawn terminator nearly all the way to the dusk terminator. The day-to-night O_2 near-surface flow begins from the same region as the SO_2 and O flows; at ~20° towards the dusk terminator. However, at the dusk terminator on the trailing hemisphere the flow now encounters the flow traveling in the opposite direction originating from the leading hemisphere's dayside. The O_2 may be driven into the ground by the condensing SO_2 flow and the plasma flux; since O_2 does not condense, it forms a buffer layer which then migrates very slowly northward in a series of nearly ballistic hops biased towards the pole at which point momentum transfer from the plasma pushes the O_2 back down onto the nightside and/or strips away and dissociates the O_2. It can be seen that the O_2 density locally increases at the dusk terminator due to this flow, an indication that the flow is real and not due to oddities with the streamlines.

Another interesting feature seen in Figure 11a (bottom panel) is the presence of a relatively low O_2 density region on the nightside of the leading hemisphere. Streamlines that enter the region travelling latitudinally swirl upon encountering the longitudinal flow from the leading hemisphere's dayside to the dusk terminator. However, because the gas is relatively collisionless on the nightside, it is unclear if the swirl streamlines are real. It is entirely possible that instead of swirling, the O_2 molecules present in the low density region are actually just bouncing repeatedly off the cold night surface until they are either stripped away or dissociated by the plasma. These features have remained persistent over several hours Io time; more detailed study with tracer particles is required to fully understand the complex rarefied flow dynamics and its interaction with the plasma.

Figure 11b shows the near surface O^+ ion density and streamlines. Recall that the upstream O^+ density in the plasma is 2400 cm^{-3} (total plasma density, including S^+ is 3600 cm^{-3}). The dense, primarily SO_2, dayside atmosphere above the subsolar region is found to prevent penetration of the plasma to low altitude. Around the edge of the dense region the plasma density is enhanced because of conservation of mass (the plasma velocity normal to the surface decreases as the plasma collides with the atmospheric column). In this high density O^+ ion region the plasma is actually fairly cold and slow due to collisions with the (still relatively dense) neutral gas. This can be seen especially in how the streamlines turn near the equator on the leading hemisphere. On the nightside the gas density is low enough that the O^+ streamlines tend to follow the field lines into the surface of Io. Note that the current model assumes that the O^+ (or S^+) incident on the surface is lost whereas in reality the ions would (eventually) be neutralized and possibly leave the surface. On the cold nightside surface, the gas species (except O_2 and possibly SO) are all expected to stick to the surface essentially indefinitely and so the assumption that a particle (not O_2 or SO) incident on the nightside is "lost" is acceptable. On the dayside, it is assumed that the particles incident on the surface (whether O^+ or O) recombine into SO_2 frost which is then sublimated based on the vapor pressure of SO_2, since the model currently assumes an infinite SO_2 reservoir. Future work should improve the surface chemistry model.

E. Steady State Atmosphere: Density

The distribution of the atmospheric component species is of great interest when attempting to model auroral emission; therefore, the species column densities and density profiles at several places in Io's atmosphere are examined in detail. Figure 12 shows the radial column density for the neutral molecular species. The dayside SO_2 gas column density is dominated by the SO_2 surface frost temperature dependence as implied by the column's clear "bulls-eye" shape about the subsolar point. Note, however, that the SO_2 column density is reduced below the hydrostatic column density at a given surface frost temperature because of photo and plasma dissociation. For example the simulated subsolar point column density ($T_s = 115$ K) is ~3.6×10^{16} cm^{-2} whereas the analytic hydrostatic column density is ~7.4×10^{16} cm^{-2}. The magnitude of this difference is surprising because the dissociation rate does not seem fast enough to result in such a low column. This difference will be explored in future work. On the nightside the analytic hydrostatic SO_2 sublimation column is 1.4×10^{12} cm^{-2} ($T_s = 90$ K) which assumes no circumplanetary winds from the dense dayside or dissociation of SO_2. Clearly, Figure 12 shows that the nightside SO_2 column is enhanced by at least a factor of 10 even with plasma dissociation, (equivalent to a surface temperature of 96.5 K in vapor pressure equilibrium), mostly due to sputtering of SO_2 off the nightside surface (see Figure 15). However, the global day-to-night winds on the leading hemisphere create a separate enhancement of the SO_2 column on the nightside extending to ~150° longitude independent of sputtering.

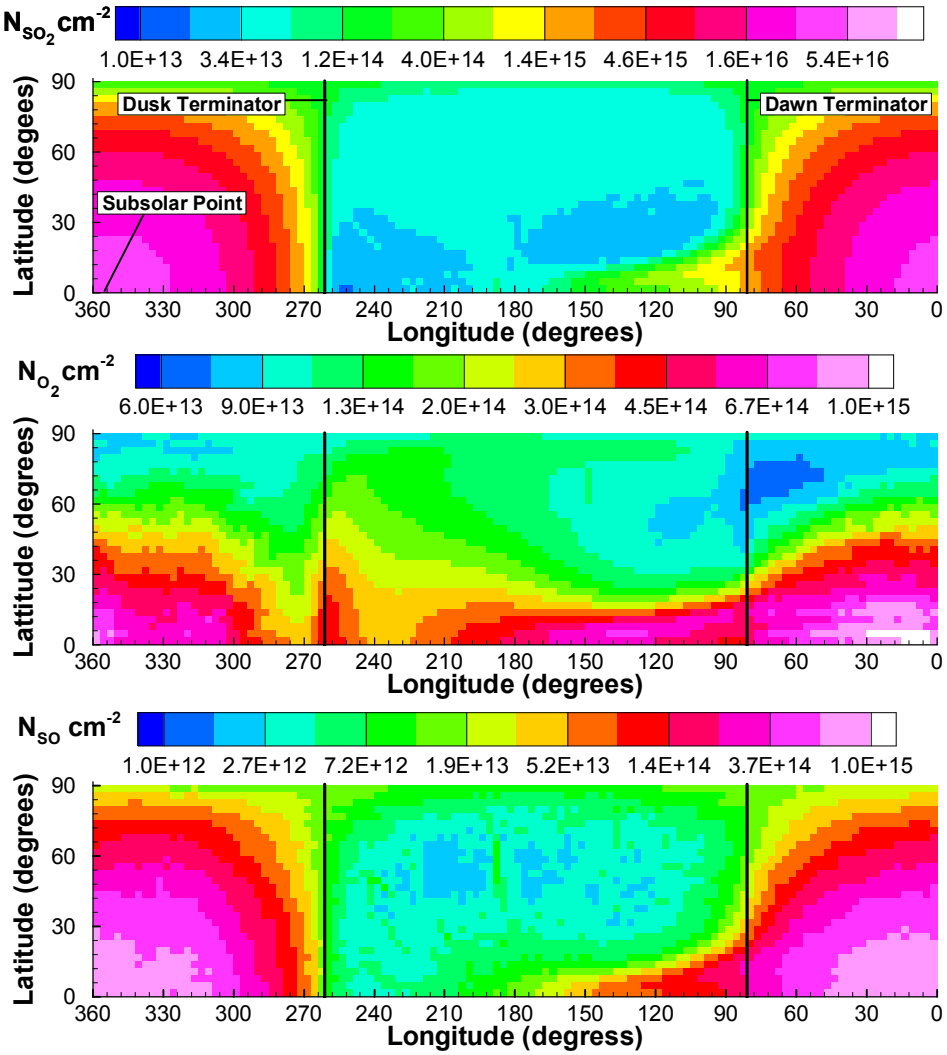

Figure 12. Color contours of the SO_2 (top), O_2 (middle), and SO (bottom) column density versus longitude and latitude. Unique contour levels for each species are used to bring out spatial details.

The buildup of non-condensable on the nightside reduces the day-to-night wind speed and pushes the condensable gases into the surface as they cross the terminator.[51,60] In the current simulations, the buildup of O_2 on the nightside[†††] influences the near surface winds in a similar way, turning the condensable gas stream into the surface. As discussed earlier, because the O_2 does not re-condense onto the surface in the current simulations, the O_2 must be either dissociated via photo-reactions (only when in sunlight) and plasma reactions or be stripped away into the plasma torus by momentum transfer or ionization. These loss rates will be examined in more detail with future simulations. Additionally, SO_2 gas molecules with large ballistic arcs rain down onto the nightside and the formation of a relatively dense O_2 nightside atmosphere (5-10 times larger column than SO_2) also helps to support the enhanced SO_2 columns. Even without sputtering, other simulations have found a similar enhancement of SO_2 on the nightside assuming both SO and O_2 are perfectly non-condensable.[54]

[†††] O_2 is almost entirely produced by photo-dissociation of SO_2, therefore the O_2 present on the nightside originated on the dayside and was then convected to the nightside where it then is slowly dissociated or stripped away by the plasma. The buildup of O_2 on the nightside is slow, and it is possible that the current simulations are not yet fully at steady state; though the O_2 densities changed very little over 2 hours.

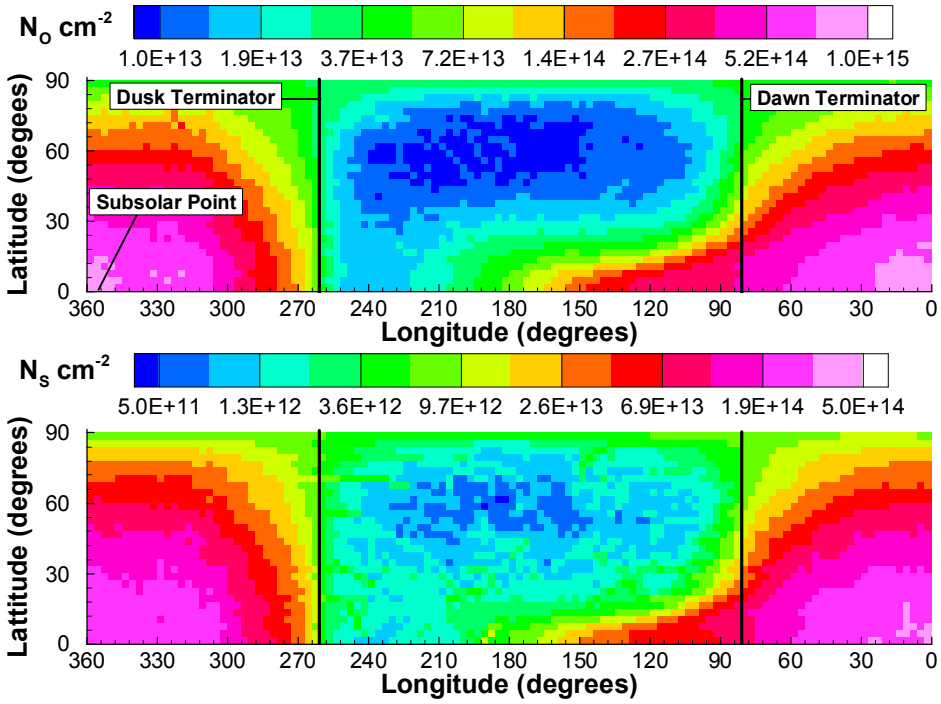

Figure 13. Color contours of the O (top) and S (bottom) column densities versus longitude and latitude. Note that the contour levels are unique for each species in order to emphasize spatial detail in each column; the S column density range is an order of magnitude wider than the O column density range.

The O_2 (middle) and SO (bottom) columns are shown in Figure 12 as well. The morphology differences in the respective columns are primarily due to the condensability of the SO (sticking probability of 0.5) in the current model. Additionally, the photo- and plasma-dissociation rates for the two species are different. The SO column essentially follows the SO_2 column on the dayside since SO_2 is the parent species; though the SO column is slightly more extended latitudinally due to the partial non-condensability of SO and the global winds. Towards the poles the SO column falls off much like SO_2 suggesting that SO production is dominated by the uniform photo-dissociation[‡‡‡] and not the pole-biased plasma-dissociation. On the other hand the O_2 column is slightly more confined to low latitudes on the dayside than the SO column; presumably the fall-off towards the pole on the dayside is due to increased plasma-dissociation of the O_2 at higher latitudes (O_2 production via SO_2 plasma-dissociation is negligible). On the nightside the O_2 is very confined to low latitudes because the day-to-night winds flow towards the equator and O_2 is mainly produced on the dayside. Currently the model does not include plasma-SO dissociation (Table 1) and therefore the SO does not exhibit the same falloff. However, the magnitude of the O_2 drop-off is exaggerated because the O_2 column contour scale does not span as large a range as the SO or SO_2 contour scales. As discussed earlier, the enhanced O_2 column near the equator is seen to extend across nearly the entire nightside and there is a buildup of O_2 at the dusk terminator where the two flows from the dayside meet and are then forced to the ground by the plasma and the condensing SO_2 flow. The O_2 column also exhibits the same low density region on the leading hemisphere seen in Figure 11a, though less defined.

The neutral atomic species column densities are shown in Figure 13. Again, on the dayside, the columns mostly follow the SO_2 column distribution, shifted latitudinally slightly due to the global winds towards the dawn terminator as seen in Figure 10b. As before, the columns are enhanced near the equator on the nightside due to the day-to-night flow across the dawn terminator. The enhanced near-equator oxygen column is seen to extend further than the enhanced sulfur column (the sulfur column density colorbar extends over a 10 times larger range than the oxygen colorbar and hence the two enhancements appear to extend nearly equally onto the nightside). The difference between the oxygen extent and the sulfur extent is due to production of oxygen via plasma dissociation of the non-condensable O_2 which dominates the nightside column. Finally, while the morphology of the oxygen and sulfur columns is relatively similar, the peak oxygen column is roughly twice the sulfur column. This is likely

[‡‡‡] The solar flux is assumed to be uniform across the dayside of Io and the gas is assumed to be optically thin.

because, ultimately, in SO_2 there are two O atoms for each S and the photo- and plasma-dissociation rates are dominated by $SO_2 \rightarrow SO+O$ and then followed by photo-dissociation of SO (see Table 2 and Figure 3).

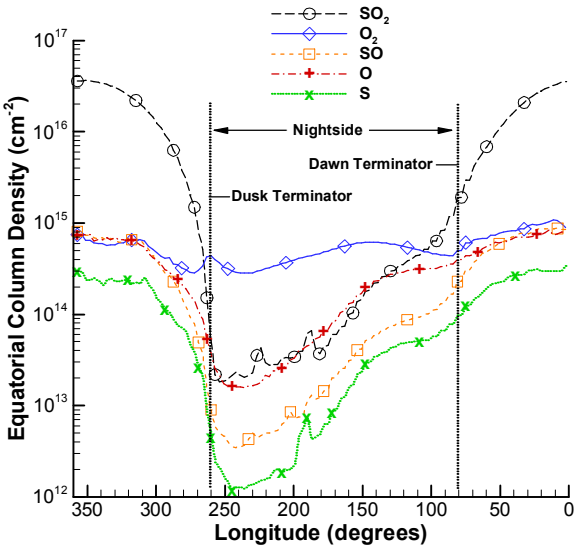

Figure 14. Extracted equatorial column densities versus longitude. The subsolar point is at 351.1° longitude; the subplasma point at 270°.

While the 2D column density plots versus longitude and latitude are useful for examining the spatial features of the various species, it is desirable to compare each species' column directly. Therefore, Figure 14 shows the column density of each neutral species versus longitude extracted from the 2D data along the equator. The SO_2 dayside column's extreme dependence on the surface temperature is obvious, as is the asymmetry between the columns on the leading (0°–180° longitude) and trailing (180°–360°) hemispheres. This asymmetry is a product of the directional plasma flow past Io which forces the day-to-night winds to flow predominately past the dawn terminator. While the O_2 column density varies very little along the equator, the O_2 column does decrease from the dayside towards the terminators and there is a local increase in the O_2 at the dusk terminator as previously discussed. However, similar local increases in the SO_2 and S columns are most likely noise since the columns are much smaller and there is noise in the sputtering yield. Finally, not only does the O_2 column exceed the SO_2 column on the nightside, but the atomic oxygen column is essentially equal to the SO_2 column over the nightside even though it is condensable. This is because the primary mechanism of oxygen production on the nightside is plasma dissociation of O_2 which dominates convection from the dayside except in the equatorial enhancement region near the dawn terminator.

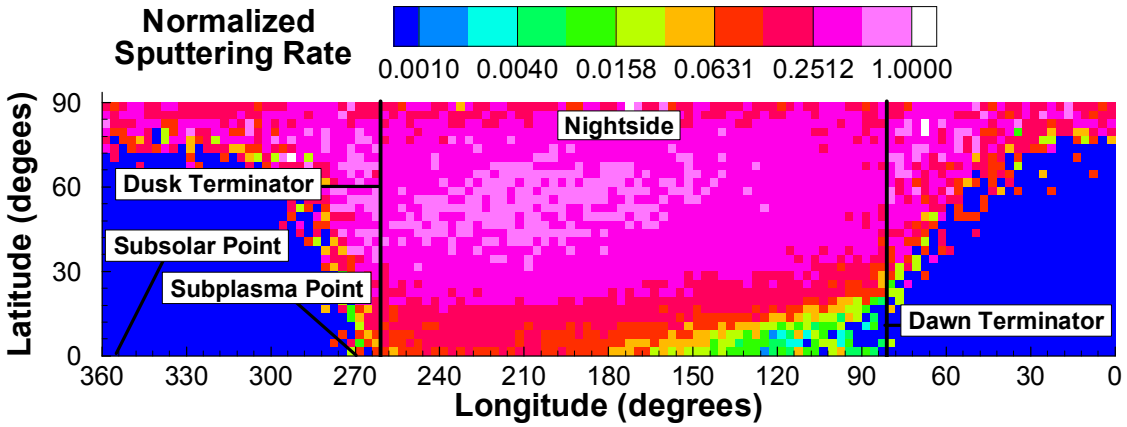

Figure 15. Color contours of the normalized SO_2 sputtering rate versus latitude and longitude.

Figure 15 shows the SO_2 sputtering rate across Io's surface normalized by the peak sputtering rate. Despite the sensitivity of the sputtering yield to the surface (frost) temperature (Figure 7), the sputtering rate is largest across the cold nightside, with a slight bias towards the trailing hemisphere which faces the oncoming plasma. The high column density over the dayside hemisphere shields the surface from the plasma (Figure 11b), preventing significant sputtering from occurring. Additionally, the plasma is shielded from reaching the surface on the nightside near the equator from the dusk terminator until ~150° longitude because the day-to-night circumplanetary winds have locally increased the column density in the intervening longitudes. In this case though, sputtering is reduced because the ion energies are reduced to near threshold via collisions with the dense neutral gas; the local ion density is actually enhanced at 4 km altitude (Figure 11b). Green auroral glows around Io, presumably due to [OI] 5577 Å and Na I 5890 Å and 5896 Å emission, have been observed which extended across the nightside but stopped at the dawn terminator.[61] It has been suggested this was possibly due to shielding of the plasma torus electrons by the remains of a dense subsolar atmosphere on the dayside even 50 minutes into eclipse.[61,62] However, if the emission is due to sputtered Na, then Figure 15 suggests that it is the suppression of sputtering by the dense dayside atmosphere due to shielding which causes the glow to stop abruptly at the dawn terminator. Atmospheric simulations which included more realistic frost maps and an SO_2 residence time model on the non-frost surface found that the dawn atmospheric column was enhanced by ~10 times over the expected frost sublimation column density due to desorption of SO_2 from the warming non-frost surface.[55] In eclipse the effect may be reduced somewhat but the presence of non-condensable O_2 should prevent the dawn atmospheric enhancement from collapse quickly.[62] This large, sharp increase in column at the dawn terminator would tend to shield the surface from sputtering more abruptly at the dawn terminator than observed in the current simulations (Figure 15) since the current uniform frost model cannot generate the dawn atmospheric enhancement. Finally, note that Na sputtered on the nightside would be unable to reach the dayside since the prevailing winds go from the high pressure dayside to the low pressure nightside.

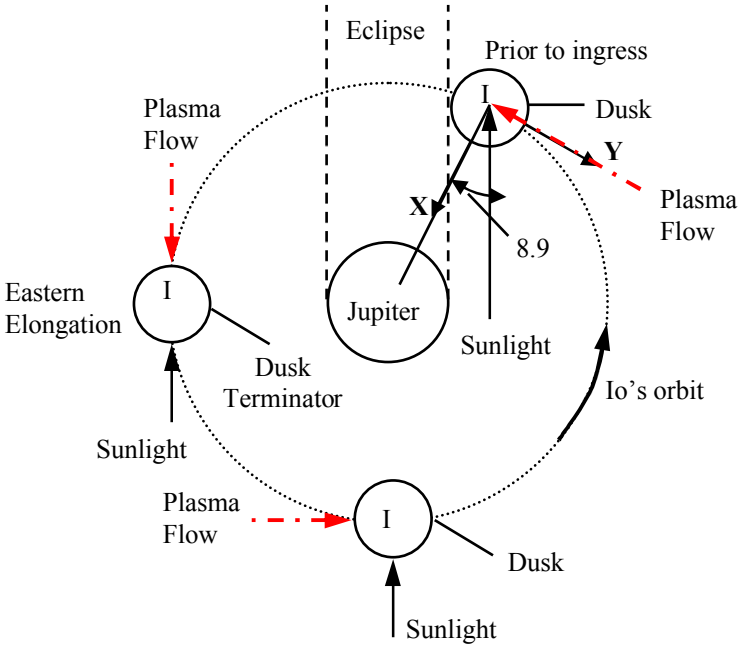

Figure 16. Schematic of Io's location in the Jovian system at various times (not to scale) and the corresponding plasma flow versus the subsolar point.

The simulation presented here has shown, among other things, the importance of the direction of the plasma flow past Io relative to the subsolar point. Figure 16 shows the changing plasma flow direction relative to the subsolar point at various points in Io's orbit. Io is just prior to ingress in the current simulation and the plasma flow is nearly directly onto the dusk terminator and perpendicular to the subsolar point. As Io orbits, the sub-plasma point does not change, but the subsolar point does. At eastern elongation the momentum transfer from the plasma flow would directly oppose the circumplanetary day-to-night winds. Similarly, when Io is in transit across Jupiter, the plasma flows onto the dawn terminator. This is almost the opposite of the current simulation and therefore it is expected that, instead of a retrograde wind, a prograde wind would develop due to the plasma pressure. The importance of the

plasma flow direction relative to the subsolar point is very intriguing and should be studied further in the future with more accurate surface models allowing for comparison to observations of Io. Finally, note that the surface from 270°–360° longitude should be preferentially scoured by plasma sputtering relative to the rest of Io's surface since the sub-plasma point is at 270° and this portion of Io's surface experiences eclipse. Eclipse by Jupiter reduces that region's local surface temperature (and thus the sublimated column) throughout the orbit because that surface region does not see a full day.[57] Since scouring of the surface frost by sputtering must occur near night time frost temperatures (day time frost temperatures result in a thick atmosphere that protects the surface from sputtering as seen in Figure 15), this reduction of the surface temperature results in a longer timeframe over which the plasma can sputter the surface. For a simple thermal surface model like the one used in the current simulations, the maximum scouring by plasma sputtering over the course of Io's orbit is expected to occur at 0° longitude which is only in sunlight for 79° of Io's orbit and in eclipse when it would otherwise be the sub-solar point. This increased sputtering might explain why the surface of Io has been observed to remain relatively frost poor from 270°–360° longitude during both the Voyager and Galileo missions.[56,63]

IV. Conclusion

In order to provide a more accurate target atmosphere for future aurora simulations, a three dimensional DSMC simulation of Io's atmosphere just prior to ingress into eclipse has been performed including photo and plasma chemistry and ion surface sputtering. Sputtering was found to be blocked over the dayside by the dense sublimation atmosphere; however, sputtering supplied most of the nightside atmosphere and peaked at higher latitudes where the ion flux was more normal to the surface. The influence of the dynamic plasma pressure on the day-to-night flow of the sublimation atmosphere was found to be quite substantial. An overall retrograde wind was formed for Io just prior to entry into eclipse. Based on these results a prograde wind would be expected for Io in transit across Jupiter. In addition, the day-to-night wind across the dawn terminator flows towards the equator due to the plasma pressure from ions streaming down the field lines and the increased nightside pressure at high latitudes. Due to the diversion of the day-to-night wind across the dawn terminator, a region of high density extends far onto the nightside near the equator (~2000 km for the condensable species), and highly asymmetric equatorial column densities result relative to the subsolar point even without thermal lag due to rotation. The apparent flow of material from high latitudes to the equator due to sputtering and the effects of the plasma on the global day-to-night winds possibly explains why the poles remain frost poor relative to the equatorial regions. The non-condensable O_2, which is a trace species on the dayside, is the dominant species on the nightside, despite increased sputtering; this is because the loss rate of O_2 due to plasma dissociation and atmospheric escape is slow. Finally, a very intriguing O_2 flow feature was observed near the dusk terminator as the flow from the leading hemisphere met the flow from the dayside trailing hemisphere. Since the O_2 does not condense on the surface, it slowly convects towards the poles where it is then free to convect back onto the nightside and eventually be dissociated or stripped away by the plasma.

Acknowledgments

This research was supported by NASA Planetary Atmospheres grants NNG05G083G, NNX11AD88G-51136, and Outer Planets Research grant NNX08AQ49G. Computations were performed at the Texas Advanced Computing Center.

References

[1]Frank, L.A., Paterson, W.R., Ackerson, K.L, Vasyliunas, V.M., Coroniti, F.V., and Bolton, S.J., 1996. Plasma observations at Io with the Galileo spacecraft. *Science* **274**, 394.

[2]Kivelson, M.G., Khurana, K.K., Russell, C.T., Joy, S.P., Volwerk, M., Walker, R.J., Zimmer, Ch., Linker, J.A., 2001. Magnetized or unmagnetized: Ambiguity persists following Galileo's encounters with Io in 1999 and 2000. *J. Geophys. Res*. **106**, 26,121–26,136.

[3]Kivelson, M.G., Bagenal, F., Kurth, W.S., Neubauer, F.M, Paranicas, C., Saur, J., 2004. Magnetospheric interactions with satellites. In: *Jupiter: The planet, Satellites and Magnetosphere* (F. Bagenal, T. Dowling, and W. McKinnon, Eds.). Cambridge University Press, Cambridge, UK, pp. 513–536.

[4]Saur, J., Neubauer, F.M., Connerney, J.E.P., Zarka, P., and Kivelson, M.G., 2004. Plasma interaction of Io with its plasma torus. In: *Jupiter: The planet, Satellites and Magnetosphere* (F. Bagenal, T. Dowling, and W. McKinnon, Eds.). Cambridge University Press, Cambridge, UK, pp. 537–560.

[5]Clarke, J.T., Ajello, J., Ballester, G., Ben Jaffel, L., Connerney, J., Gérard, J.-C., Gladstone, G.R., Grodent, D., Pryor, W., Trauger, J., and Waite Jr, J.H., 2002. Ultraviolet emissions from the magnetic footprints of Io, Ganymede and Europa on Jupiter. *Nature* **415**, 997–1000.

[6]Bigg, E.K.,1964. Influence of the satellite Io on Jupiter's decametric emission. *Nature* **203**, 1008–1010.
[7]Schneider, N.M. and Trauger, J.T., 1995. The structure of the Io torus. *Astrophys. J.* **450**, 450–462.
[8]Delamere, P.A. and Bagenal, F., 2005. Radial variations in the Io plasma torus during the Cassini era. *J. Geophys. Res.* **110**, A12223.
[9]Sittler, E.C., and D.F. Strobel 1987. Io plasma torus electrons – Voyager 1. *J. Geophys. Res*. **92**, 5,741–5762.
[10]Smyth, W.H. and Marconi, M.L., 1998. An explanation for the east–west asymmetry of the Io plasma torus. *JGR* **103**, No. A5, 9091–9100.
[11]Spencer, J.R. and Schneider, N.M., 1996. Io on the eve of the Galileo mission. *Annu. Rev. Earth Planet. Sci.* **24**, 125–190.
[12]Linker, J.A., M.G. Kivelson, and R.J. Walker, 1991. A three-dimensional MHD simulation of plasma flow past Io. *J. Geophys.Res*. **96**, 21,037–21,053.
[13]Linker, J. A., K.K. Khurana, M.G. Kivelson, and R.J. Walker, 1998. MHD simulation of Io's interaction with the plasma torus. *J. Geophys. Res.* **103**, 19,867–19,877.
[14]Combi, M.R., K. Kabin, T.I. Gombosi, and D.L. De Zeeuw, 1998. Io's plasma environment during the Galileo flyby: Global three-dimensional MHD modeling with adaptive mesh refinement. *J. Geophys. Res*. **103**, 9,071-9,081.
[15]Saur, J., F. M. Neubauer, D. F. Strobel, and M. E. Summers, 1999. Three-dimensional plasma simulation of Io's interaction with the Io plasma torus: Asymmetric plasma flow. *J. Geophys. Res.* **104**, 25,105–25,126.
[16]Neubauer, F.M., 1980. Nonlinear standing Alfvén wave current system at Io: Theory. *J. Geophys. Res.* **85**, A3, 1171–1178.
[17]Saur, J., Neubauer, F.M., Strobel, D.F., Summers, M.E., 2000. Io's ultraviolet aurora: Remote sensing of Io's interaction. *GRL* **27**, 2893-2896.
[18]Saur, J., F.M. Neubauer, D.F. Strobel, and M.E. Summers, 2002. Interpretation of Galileo's Io plasma and field observations: The J10, I24, I27 flybys, and close polar passes. *J. Geophys. Res*. **107**, A12, 5-1.
[19]Lipatov A.S. and Combi, M.R., 2006. Effects of kinetic processes in shaping Io's global plasma environment: A 3D hybrid model. *Icarus* **180**, 412–427.
[20]Dols, V., Delamere, P.A., and Bagenal, F., 2008. A multispecies chemistry model of Io's local interaction with the plasma torus. *J. Geophys. Res.* **113**, A09208.
[21]Stewart, B.D., 2010. PhD dissertation, The University of Texas at Austin. Numerical simulations of the flow produced by a comet impact on the Moon and its effects on ice deposition in cold traps.
[22]Bird, G.A., 1985. Low density aerothermodynamics, AIAA paper 85–0994.
[23]Chen, F.F., 1984. *Introduction to plasma physics and controlled fusion Volume 1: Plasma physics.* Springer–Verlag, New York.
[24]Birdsall, C.K. and Langdon, A.B., 2005. *Plasma Physics via Computer Simulation.* Taylor & Francis Group, New York.
[25]Bose, D. and Candler, G.V., 1996. Thermal rate constants of the N_2+O→NO+N reaction using *ab initio* $^3A''$ and $^3A'$ potential energy surfaces. *J. Chem. Phys.* **104**, 2825–2833.
[26]Ozawa, T., Levin, D.A., and Wysong, I.J., 2007. Chemical reaction modeling for hypervelocity collisions between O and HCl. *Phys. of Fluids* **19**, 056102.
[27]Bird, G.A., 1994. *Molecular Gas Dynamics and the Direct Simulation of Gas Flows*. Oxford Univ. Press, Oxford.
[28]Deng, H., Moore, C.H., Levin, D.A., Goldstein, D.B., and Varghese, P.L. Analysis of SO_2+O chemistry models for simulations of the atmosphere of Io. *Proceedings of the 27th International Rarefied Gas Dynamics Symposium.* **1033**, 1139–1144.
[29]Parsons, N., Levin, D.A., 2012. Development of a Chemistry Model for DSMC Simulation of the Atmosphere of Io. *50th AIAA Aerospace Sciences Meeting including the New Horizons Forum and Aerospace Exposition*. Nashville, TN.
[30]Johnson, R.E., Liu, M., and Tully, C., 2002. Collisional dissociation cross sections for O + O_2, CO and N_2, O_2 + O_2, N + N_2, and N_2 + N_2. *Planet. Space Sci.* **50**, 123–128.
[31]Smirnov, B.M., 2000. Tables for cross sections of the resonant charge exchange process. *Phys. Scripta* **61**, 595–602.
[32]Singleton and Cvetanovic, 1988. Evaluated chemical kinetic data for the reactions of atomic Oxygen O(^{3}P) with Sulfur containing compounds. *J. Phys. Chem. Ref. Data* **17**, No. 4, 1377–1437.
[33]Haff, P.K., Watson, C.C., and Yung, Y.L., 1981. Sputter Ejection of Matter from Io. *JGR* **86**, No. A8, 6933–6938.
[34]Lanzerotti, L.J., Brown, W.L., Augustyniak, W.M., Johnson, R.E., and Armstrong, T.P., 1982. Laboratory studies of charged particle erosion of SO_2 ice and applications to the frosts of Io. *Astrophys. J.* **259**, 920–929.
[35]Cheng, A.F., 1984. Escape of Sulfur and Oxygen from Io. *JGR* **89**, No. A6, 3939–3944.
[36]Melcher, C.L., LePoire, D.J., Cooper, B.H., and Tombrello, T.A., 1982. Erosion of frozen sulfur dioxide by ion bombardment: Applications to Io. *Geophys. Res. Lett.* **9**, No. 10, 1151–1154.
[37]Boring, J.W., Johnson, R.E., Reimann, C.T., Garrett, J.W., Brown, W.L., and Marcantonio, J.W., 1983. Ion induced chemistry in condensed gas solids. *Nucl. Instrum. Methods*, **218**, 707–711.
[38]Boring, J.W., Garrett, J.W., Cummings T.A., Johnson, R.E., and Brown, W.L., 1984. Sputtering of solid SO_2. *Nucl. Instrum. Methods, B1*, 321–326.
[39]Johnson, R.E., 1990. *Energetic charged particle interactions with atmospheres and surfaces*. Springer–Verlag, Berlin.
[40]Sigmund, P., 1969. Theory of sputtering. I: Sputtering yield of amorphous and polycrystalline targets. *Phys. Rev.* **184**, No. 2, 383–416.
[41]Johnson, R.E., Garrett, J.W., Boring, J.W., Barton, L.A., and Brown, W.L., 1984. Erosion and modification of SO_2 ice by ion bombardment of the surface of Io. *JGR* **89**, B711–B715.
[42]Chrisey, D.B., Johnson, R.E., Phipps, J.A., McGrath, M.A., and Boring, J.A., 1987. Sputtering of sulfur by kiloelectronvolt ions: Application to the magnetospheric plasma interaction with Io. *Icarus* **70**, 111–123.
[43]Brown, W.L., Lanzerotti, L.J., and Johnson, R.E., 1982. , *Science* **218**, 525.

[44]Johnson, R.E., 2011. *Private communications.*
[45]Strobel, D.F. and Wolven, B.C., 2001. The atmosphere of Io: Abundances and sources of Sulfur dioxide and atomic hydrogen. *Astrophys. Space Sci.*, **277**, 271–281.
[46]Feaga, L.M., McGrath, M.A, and Feldman, P.D., 2009. Io's dayside SO_2 atmosphere. *Icarus* **201**, 570-584.
[47]Sieveka, E.M. and Johnson, R.E., 1985. Nonisotropic coronal atmosphere on Io. *JGR* **90**, No. A6, 5327–5331.
[48]McGrath, M.A. and Johnson, R.E., 1987. Magnetospheric plasma sputtering of Io's atmosphere. *Icarus* **69**, 519–531.
[49]Moore, C.H., 2011. PhD dissertation, The University of Texas at Austin. Monte Carlo simulation of the Jovian plasma torus interaction with Io's atmosphere and the resultant aurora during eclipse.
[50]Summers, M.E. and Strobel, D.F., 1996. Photochemistry and Vertical Transport in Io's Atmosphere and Ionosphere. *Icarus* **120**, 290–316.
[51]Austin, J.V. and Goldstein, D.B. 2000. Rarefied Gas Model of Io's Sublimaion Driven Atmosphere. *Icarus* **148**, 370-383.
[52]Carlson, R.W., Kargel, J.S., Douté, S., Soderblom, L.A., and Dalton, J.B., 2006. Io's surface composition. In: *Io after Galileo* (R. Lopes and J. Spencer, Eds.). Spinger, Chichester, UK, pp. 231–264.
[53]Huebner, W.F., Keady, J.J., and Lyon, S.P., 1992. Solar photo rates for planetary atmospheres and atmospheric pollutants. *Astrophysics and Space Science*, **195**, 1–294.
[54]Wong, M.C. and W.H. Smyth, 2000. Model calculations for Io's atmosphere at Eastern and Western elongation. *Icarus* **146**, 60-74.
[55]Walker, A. C., Gratiy, S. L., Goldstein, D. B., Moore, C. H., Varghese, P. L., Trafton, L. M., Levin, D. A., and Stewart, B. D., 2010a. A Comprehensive Numerical Simulation of Io's Sublimation-Driven Atmosphere. *Icarus* **207**, 409–432.
[56]Douté, S., Schmitt B., Lopes-Gautier R., Carlson, R., Soderblom, L., Shirley, J., and the Galileo NIMS Team. Mapping SO_2 frost on Io by the modeling of NIMS hyperspectral images. *Icarus* **149**, 107–132.
[57]Walker, A.C., Goldstein, D.B., Varghese, P.L., Trafton, L.M., and Moore, C.H., 2010b. Simulated Ionian Column Densities. *DPS 42*, #26.11.
[58]Moullet, A., Lellouch, E., Moreno, R., Gurwell, M.A., and Moore, C.H., 2008. First disk-resolved millimeter observations of Io's surface and SO_2 atmosphere. *A&A* **482**, 279–292.
[59]Smyth, W.H. and M.C. Wong, 2004. Impact of electron chemistry on the structure and composition of Io's atmosphere. *Icarus* **171**, 171–182.
[60]Wong, M.C. and Johnson, R.E., 1996. A Three-Dimensional Azimuthally Symmetric Model Atmosphere for Io 1. Photochemistry and the Accumulation of a Nightside Atmosphere. *JGR* **101**, 23,243-23,254.
[61]Geissler, P., McEwen, A., Ip, W., Belton, M., Johnson, T., Smyth, W., and Ingersoll, A., 1999. Galileo Imaging of Atmospheric Emissions from Io. *Science* **285**, 870-874.
[62]Moore, C.H., Goldstein, D.B., Varghese, P.L., Trafton, L.M., and Stewart, B., 2009. 1-D DSMC simulation of Io's atmospheric collapse and reformation during and after eclipse. *Icarus* **201**, 585–597.
[63]McEwen, A.S., Johnson, T.V., Matson, D.L., and Soderblom, L.A., 1988. The global distribution, abundance, and stability of SO_2 on Io. *Icarus* **75**, 450–478.